Copy 344
RM L55A31

NACA RM L55A31

NACA

CASE FILE
COPY

RESEARCH MEMORANDUM

LATERAL STABILITY CHARACTERISTICS AT LOW LIFT BETWEEN MACH NUMBERS OF 0.85 AND 1.15 OF A ROCKET-PROPELLED MODEL OF A SUPERSONIC AIRPLANE CONFIGURATION HAVING A TAPERED WING WITH CIRCULAR-ARC SECTIONS AND 40° SWEEPBACK

By Charles T. D'Aiutolo and Allen B. Henning

Langley Aeronautical Laboratory
Langley Field, Va.

CLASSIFICATION CHANGED TO UNCLASSIFIED
AUTHORITY: NACA RESEARCH ABSTRACT NO. 128
EFFECTIVE DATE: JUNE 24, 1958
WHL

CLASSIFIED DOCUMENT

This material contains information affecting the National Defense of the United States within the meaning of the espionage laws, Title 18, U.S.C., Secs. 793 and 794, the transmission or revelation of which in any manner to an unauthorized person is prohibited by law.

NATIONAL ADVISORY COMMITTEE
FOR AERONAUTICS

WASHINGTON
April 28, 1955

NATIONAL ADVISORY COMMITTEE FOR AERONAUTICS

RESEARCH MEMORANDUM

LATERAL STABILITY CHARACTERISTICS AT LOW LIFT BETWEEN MACH NUMBERS OF 0.85 AND 1.15 OF A ROCKET-PROPELLED MODEL OF A SUPERSONIC AIRPLANE CONFIGURATION HAVING A TAPERED WING WITH CIRCULAR-ARC SECTIONS AND 40° SWEEPBACK

By Charles T. D'Aiutolo and Allen B. Henning

SUMMARY

A rocket-propelled model of a supersonic airplane configuration employing a 40° sweptback wing having circular-arc sections was flight tested in the Mach number range of 0.85 and 1.15 to obtain lateral stability data at low lift from the lateral response to an impulsive rudder deflection and to evaluate the test and analysis technique.

Time histories of the Dutch-roll oscillations indicate that the model was statically stable throughout the Mach number range but was dynamically unstable over a small range of Mach numbers. A low-lift buffet was experienced below a Mach number of 0.95.

The time-vector method applied to the recorded Dutch-roll transient oscillations provided a useful method for the determination of the lateral stability derivatives. The results as obtained from the vector analysis indicate that the directional stability and effective dihedral increased with increasing Mach number, the damping-in-yaw was low and over a small region of Mach number was unstable, and the rate of change of rolling-moment coefficient with yawing-angular-velocity factor was negative at a Mach number of 0.89 and increased positively to a large positive value at a Mach number of 1.1. The lateral-force derivative increased with increasing Mach number until a Mach number of 0.98 and then decreased to the limit Mach number of the test.

Comparisons between the rocket-propelled-model test data, wind-tunnel data, and estimates were made in order to evaluate the test technique. These comparisons indicated that the time-vector method allows the

determination of the static lateral stability derivatives to the same order of accuracy as does wind-tunnel techniques.

INTRODUCTION

The Pilotless Aircraft Research Division is conducting a flight investigation to determine the longitudinal and lateral stability characteristics at low lift in the transonic speed range of a supersonic airplane configuration having a tapered wing with circular-arc sections and 40° sweepback. The longitudinal stability characteristics of the configuration are presented in reference 1 and the present paper contains the results from a flight to determine the lateral stability characteristics. The Mach number range covered in the present test was from 0.85 to 1.15 and corresponds to a Reynolds number range of 7.3×10^6 to 9.8×10^6, respectively. The model was flown at the Langley Pilotless Aircraft Research Station at Wallops Island, Va.

Stability derivatives were determined by application of the time-vector method (see refs. 2 to 6) and these derivatives are compared with other tests and with the estimated values of the stability derivatives in order to evaluate the test technique. The physical motions experienced by the model may or may not be the same as those experienced by the airplane since the model and airplane would have different mass and inertia characteristics.

SYMBOLS AND COEFFICIENTS

Throughout this paper the forces and moments acting on the model are referred to the body system of axes, which are defined as an orthogonal system of axes intersecting at the airplane center of gravity, in which the Z-axis is in the plane of symmetry and perpendicular to the X-axis. The X-axis is in the plane of symmetry, and the Y-axis is perpendicular to the plane of symmetry. A diagram of these axes showing the positive direction of forces, moments, and angles is presented in figure 1. Since aerodynamic derivatives are usually available relative to the stability system of axis, a diagram showing the stability system of axis is included in figure 1 for reference purposes.

Reference 7 gives expressions that can be used to transpose the aerodynamic derivatives from one system of axes to the other. Angular relationships in flight for the stability and body systems of axes indicating positive directions of angles is presented in figure 2.

The symbols and coefficients are defined as follows:

A	aspect ratio
A_l/g	acceleration along X reference axis as obtained from accelerometer, positive forward
A_n/g	acceleration normal to X reference axis as obtained from accelerometer, positive up
A_T/g	acceleration along Y reference axis as obtained from accelerometer, positive to the right
a	total damping factor (logarithmic decrement of Dutch-roll oscillation defined as being a positive number for a damped oscillation)
b	wing span, ft
c	wing chord, ft
$\bar{c}_w$	mean aerodynamic chord of wing, ft
$\bar{c}_{vt}$	mean aerodynamic chord of vertical tail, ft
D	differential operator, d/dt
I_X	moment of inertia about body X-axis, slug-ft^2
I_Z	moment of inertia about body Z-axis, slug-ft^2
I_{XZ}	product of inertia referred to body axis (positive when the positive direction of the X principal axis is inclined below reference axis, that is, when ϵ is positive) $\frac{1}{2}\left[I_Z - I_X\right]\tan 2\epsilon$
L	rolling moment, ft-lb
M'	pitching moment, ft-lb
N	yawing moment, ft-lb
M	Mach number
m	mass of model, slugs

P	period of Dutch-roll oscillations, sec
p	rolling angular velocity about X-axis, radians/sec
P_T	total stagnation pressure, lb/sq ft
q	dynamic pressure, $\frac{1}{2}\rho V^2$, lb/sq ft
R	Reynolds number
r	yawing angular velocity about Z-axis, radians/sec
S	total wing area, sq ft
t_h	one-half thickness of airfoil at aileron hinge line, as shown in figure 3(b).
t	time, sec
V	velocity, ft/sec
W	model weight, lb
ρ	air density, slugs/cu ft
μ	relative density factor, $\frac{m}{\rho S b}$
ω_o	undamped natural circular frequency, $(\omega^2 + a^2)^{1/2}$ radians/sec
ω	frequency of the Dutch-roll oscillation, radians/sec
α	angle in plane of symmetry, measured from projection of relative wind to fuselage reference axis, deg or radians (see fig. 2)
β	angle of sideslip, measured from relative wind to fuselage reference axis, deg or radians (see fig. 1)
ϵ	angle between principal longitudinal axis of inertia and the longitudinal body axis, deg, (see fig. 2)
γ	flight path angle, deg, (see fig. 2)
θ	angle between reference axis and horizontal axis, deg, (see fig. 2)

η inclination of principal longitudinal axis of inertia with respect to flight path, deg, (see fig. 2)

ϕ angle of roll, radians

ψ angle of yaw, radians

δ_r rudder deflection, deg

Φ phase angle, deg

C_L trim lift coefficient

C_Y lateral-force coefficient, Lateral force/qS

C_n yawing-moment coefficient, Yawing moment/qSb

C_l rolling-moment coefficient, Rolling moment/qSb

C_{n_β} directional stability derivative, $\frac{\partial C_n}{\partial \beta}$, per radian

C_{Y_β} lateral-force derivative, $\frac{\partial C_Y}{\partial \beta}$, per radian

C_{l_β} effective dihedral derivative, $\frac{\partial C_l}{\partial \beta}$, per radian

C_{n_p} rate of change of yawing-moment coefficient with rolling-angular-velocity factor, $\frac{\partial C_n}{\partial \frac{pb}{2V}}$, per radian

C_{Y_p} rate of change of lateral-force coefficient with rolling-angular-velocity factor, $\frac{\partial C_Y}{\partial \frac{pb}{2V}}$, per radian

C_{l_p} damping-in-roll derivative, $\frac{\partial C_l}{\partial \frac{pb}{2V}}$, per radian

C_{n_r} rate of change of yawing-moment coefficient with yawing-angular-velocity factor, $\frac{\partial C_n}{\partial \frac{rb}{2V}}$, per radian

C_{Y_r} rate of change of lateral-force coefficient with yawing-angular-velocity factor, $\frac{\partial C_Y}{\partial \frac{rb}{2V}}$, per radian

C_{l_r} rate of change of rolling-moment coefficient with yawing-angular-velocity factor, $\frac{\partial C_l}{\partial \frac{rb}{2V}}$, per radian

$C_{n_{\dot{\beta}}}$ rate of change of yawing-moment coefficient with rate of change of angle-of-sideslip factor, $\frac{\partial C_n}{\partial \frac{\dot{\beta}b}{2V}}$, per radian

$C_{Y_{\dot{\beta}}}$ rate of change of lateral-force coefficient with rate of change of angle-of-sideslip factor, $\frac{\partial C_Y}{\partial \frac{\dot{\beta}b}{2V}}$, per radian

$C_{l_{\dot{\beta}}}$ rate of change of rolling-moment coefficient with rate of change of angle-of-sideslip factor, $\frac{\partial C_l}{\partial \frac{\dot{\beta}b}{2V}}$, per radian

The symbol $|j|$ represents the absolute magnitude of j and is always taken to be positive. A dot over a variable indicates the first derivative of the variable with respect to time. Two dots indicate the second derivative. Phase angles are indicated by subscript notation as $\Phi_{\ddot{\phi}\beta}$ as the phase angle between sideslip and rolling angular acceleration. The second subscript symbol is used as the reference. A positive sign associated with the phase angle indicates that the first subscript symbol leads the reference, whereas a negative sign indicates that the first subscript symbol lags the reference.

MODEL AND TEST DESCRIPTION

Model Description

The general arrangement of the model, details of wing and tail, and details of rudder are shown in figure 3, and the geometric and mass characteristics of the model are given in table I. Photographs of the model and the model-booster combination are shown in figure 4.

The model fuselage was a body of revolution of fineness ratio 9.58, consisting of a cylindrical center section, ogival nose and tail sections, dorsal fin, canopies, and fuselage skid. Construction of the fuselage was principally of aluminum covered with magnesium skin.

The nose section contained the telemeter; the center section contained the power section and wing mount; and the tail section contained the rudder-pulsing mechanism.

The wing of the model was made of steel and had 10-percent circular-arc airfoil sections perpendicular to the quarter-chord line and incorporated 40° of sweepback at the quarter-chord line with 3° positive dihedral. The wing was set at 3° incidence with respect to the fuselage reference line and was modified to simulate slab-sided ailerons having a trailing-edge thickness of one-half the aileron thickness at the hinge line. The ailerons were of 25-percent span and were constructed (or set) at 0° deflection. Tip fairings were placed on the wing in order to house some of the instrumentation.

The horizontal tail was similar to the wing in plan form but had NACA 65-008 airfoil sections parallel to the fuselage reference line and was constructed of aluminum. An incidence of 2° trailing edge down relative to the fuselage reference line was set in the horizontal tail so that the model would have reasonable trim values. (See ref. 1).

The vertical tail had NACA 27-010 airfoil sections parallel to fuselage reference line at the root and NACA 27-008 airfoil sections parallel to fuselage reference line at the tip and was constructed of aluminum. An aluminum rudder, the details of which are shown in figure 3(c), was incorporated on the vertical tail and was used to disturb the model in yaw.

The model rudder-pulsing mechanism was designed to deflect the rudder impulsively between 0° and 25° by means of a hydraulic servo system and then allow a dwell time before the rudder was deflected again. The time required to move the rudder from 0° to the maximum deflection of 25° and then back to 0° was 0.07 second and the dwell time was about 0.54 second; thus, a complete cycle occurred every 0.61 second.

The model was boosted to a Mach number of 1.18 by an external ABL Deacon rocket motor. Upon burnout of this rocket motor, the model separated from the booster and coasted through the test speed range (data obtained from M = 1.15). The model-booster combination was launched from a mobile launcher at an angle of about 45° as shown in figure 4(c).

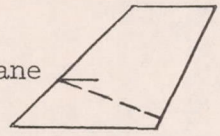
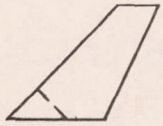
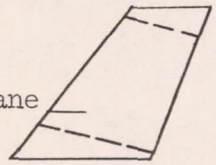
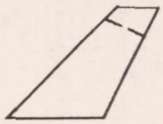
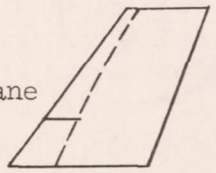
Instrumentation

The model contained a standard twelve-channel NACA telemeter. Measurements were made of the normal, longitudinal, and transverse accelerations near the center of gravity of the model and the normal and transverse accelerations in the nose of the model. Normal accelerations of each wing tip were measured in order to determine the rolling angular acceleration of the model. Rolling angular accelerations were also measured by an angular-accelerometer-type instrument. The angle of attack and angle of sideslip were measured by a vane-type instrument located on a sting forward of the nose of the model, whereas total pressure was measured by a tube located on a small strut mounted on the underside of the model near the nose and rudder deflections were measured by a control-position pickup.

The position of the model in space was determined by use of a modified SCR 584 tracking radar set and the velocity of the model was obtained by use of the CW Doppler velocimeter radar set. Atmospheric data were obtained from a radiosonde released immediately before the model flight. Fixed and tracking motion-picture cameras were used to observe the condition of the model during most of the flight.

Preflight Test

Prior to flight testing, the model was suspended by shock cords and shaken by means of an electromagnetic shaker. This preflight test was performed in anticipation of the model experiencing high-frequency oscillations during the flight; thereby, an explanation of these high-frequency oscillations was possible. The frequencies recorded in the shake tests of the model together with the approximate nodal lines are tabulated on the following page.

Mode	Nodal line	Frequency, cps
Wing first bending		49
Horizontal-tail first bending		86
Wing second bending		176
Horizontal-tail second bending		336
Wing torsion		262

Flight Test

The model was boosted to a Mach number of 1.18 and upon burnout of the booster rocket motor the model separated from the booster. During the boosted phase of the flight, the rudder-pulsing mechanism was

inoperative and was not allowed to operate until the model was completely separated from the booster (M = 1.15). After completely separating from the booster, the model was disturbed in yaw by periodic pulses of the rudder and time histories of the resulting model motions were obtained by means of the NACA telemeter and instrument system.

The flight conditions of the model are presented in figure 5 where the variation of air density, velocity, dynamic pressure, and relative density factor with Mach number are shown. These quantities are presented so that a possible correlation of the data obtained from this test with data obtained from other tests may be made. The range of the Reynolds numbers of the present test is shown in figure 6.

ACCURACY AND CORRECTIONS

Accuracy

The estimated probable errors in the basic quantities measured are shown in table II. The lateral stability derivatives C_{Y_β}, C_{n_β}, C_{l_β}, C_{l_r}, and $C_{n_r} - C_{n_{\dot{\beta}}}$ are dependent upon some of or all these measured quantities. The probable error in any of the above derivatives due to all the probable errors in table II was determined by the method shown in reference 2 and it is felt that the accuracy of the derivatives reported in this paper are of the same order as those reported in reference 2. That is, at M = 1.1 and M = 0.9 the accuracies are, respectively: 3 and 5 percent for C_{Y_β}, 6 and 8 percent for C_{n_β} and C_{l_β}, 13 and 16 percent for C_{l_r}, and 15 and 25 percent for $C_{n_r} - C_{n_{\dot{\beta}}}$.

It is believed that the data presented in this report provide a good indication of the variation of the stability derivatives with Mach number, and the absolute values of these derivatives are at least as accurate or better than indicated above.

Corrections

Since it was impossible to mount the accelerometers exactly at the center of gravity of the model, the accelerometer readings had to be corrected so that the accelerations of the center of gravity of the model could be determined. These corrections consisted of the linear and angular acceleration effects as well as angular velocity effects on the accelerometer readings due to the model motions.

The angles of attack and sideslip as measured in front of the model were corrected to the model center of gravity by considering flight path curvature effects, see reference 8.

Frequency-response corrections to all instruments except the angular accelerometer were not necessary since the model natural frequency was less than 4 percent of the instrument natural frequency. Frequency-response corrections, however, were applied to the angular-accelerometer readings since the model natural frequency was as high as 20 percent of the angular-accelerometer natural frequency. These corrections were made by use of standard frequency-response charts and resulted in corrections to the phase angle only. The frequency-response corrections to the phase angle between the rolling angular acceleration and sideslip angle amounted to 9.6° at $M = 0.89$ and 16.3° at $M = 1.10$.

ANALYSIS

The method used in this paper to analyze the data and to determine the lateral stability derivatives C_{l_β}, C_{n_β}, C_{l_r}, and $C_{n_r} - C_{n_{\dot{\beta}}}$ is based on the concept of rotating vectors. This concept as applied to airplane dynamics was first formulated by Mueller (see ref. 3) and extended by others (see refs. 4 to 6) and may be briefly described as follows:

A fundamental property of rotating or time vectors is the relationship between the vector and its derivatives or its integrals at a given instant of time. This relationship may be illustrated by considering the oscillatory motions resulting from a yaw disturbance which are assumed to be given by

$$\beta = \beta_o e^{-at} \cos \omega t \tag{1}$$

$$\psi = \frac{|\psi|}{|\beta|} \beta_o e^{-at} \cos\left(\omega t + \Phi_{\psi\beta}\right) \tag{2}$$

$$\phi = \frac{|\phi|}{|\beta|} \beta_o e^{-at} \cos\left(\omega t + \Phi_{\phi\beta}\right) \tag{3}$$

Differentiation of equation (3) gives

$$\dot{\phi} = \sqrt{a^2 + \omega^2}\, \frac{|\phi|}{|\beta|} \beta_o e^{-at} \cos\left(\omega t + \Phi_{\phi\beta} + 90^\circ + \tan^{-1}\frac{a}{\omega}\right) \tag{4}$$

whereas the second differentiation of equation (3) yields

$$\ddot{\phi} = \left(a^2 + \omega^2\right) \frac{|\phi|}{|\beta|} \beta_o e^{-at} \cos\left(\omega t + \Phi_{\phi\beta} + 180^\circ + 2 \tan^{-1} \frac{a}{\omega}\right) \qquad (5)$$

where ω is the frequency at which these vectors are rotating and β_o is the initial value of the sideslip angle.

Differentiation of equations (1) and (2) yields similar expressions.

Comparisons of equations (3) and (4) show that the amplitude of the first derivative of a time vector is equal to the amplitude of the time vector at the same instant of time multiplied by the undamped natural circular frequency of the vector, and that the phase of the first derivative leads the time vector by $90^\circ + \tan^{-1} \frac{a}{\omega}$ where $\tan^{-1} \frac{a}{\omega}$ is referred to as the damping angle.

Comparison of equations (3) and (5) shows that the amplitude of the second derivative of a time vector is equal to the amplitude of the time vector multiplied by the square of the undamped natural circular frequency of the vector, and that the phase of the second derivative leads the time vector by 180° plus twice the damping angle.

In a like manner, the amplitude of the integral of a time vector may be shown to be equal to the time vector divided by the undamped natural circular frequency, whereas the phase of the integral of a time vector lags the time vector 90° plus the damping angle.

Another important property of the concept of time vectors is the requirement that the vector polygon representing any degree of freedom of a system must close; thereby the determination of only two unknown quantities in the degree of freedom is allowed. This property will be explained in detail under the discussion of the solution of the lateral equations of motion.

The complete lateral equations of motion about fixed body axis (see fig. 1) are:

Lateral force:

$$\frac{mV}{qS}(D\beta + D\psi - \alpha D\phi) = C_{Y_\beta}\beta + C_{Y_p} \frac{b}{2V} D\phi + C_{Y_r} \frac{b}{2V} D\psi + C_{Y_{\dot{\beta}}} \frac{b}{2V} D\beta +$$

$$\frac{W}{qS} (\phi \cos \theta + \psi \sin \theta) \qquad (6)$$

Rolling moment:

$$\frac{I_X}{qSb} D^2\phi - \frac{I_{XZ}}{qSb} D^2\psi = C_{l_\beta}\beta + C_{l_p} \frac{b}{2V} D\phi + C_{l_r} \frac{b}{2V} D\psi + C_{l_{\dot{\beta}}} \frac{b}{2V} D\beta \quad (7)$$

Yawing moment:

$$\frac{I_Z}{qSb} D^2\psi - \frac{I_{XZ}}{qSb} D^2\phi = C_{n_\beta}\beta + C_{n_p} \frac{b}{2V} D\phi + C_{n_r} \frac{b}{2V} D\psi + C_{n_{\dot{\beta}}} \frac{b}{2V} D\beta \quad (8)$$

Assumptions were made concerning some of the terms in these equations in order to facilitate analysis of the data. These assumptions are: In the lateral-force equation all the aerodynamic terms are combined into one term referred to as C_Y or the total lateral force. This assumption is valid since the total lateral force was measured by a transverse accelerometer and includes the contributions of rolling angular velocity, yawing angular velocity, and sideslip angle. It was further assumed that C_Y was equal to $C_{Y_\beta}\beta$. The validity of this assumption is shown from the time history of the model motions where C_Y is within the limits of accuracy of the test 180° out of phase with the sideslip angle β. It was also assumed that the gravity terms in the lateral-force equation may be neglected. This assumption is valid for rocket-propelled models since the models have low wing loadings and are flown through rather dense air at high speeds so that the values of the gravity terms are very small. In the rolling-moment equation it was assumed that $C_{l_{\dot{\beta}}} = 0$, whereas in the yawing-moment equation it was assumed that $\psi = -\beta$, so that C_{n_r} and $C_{n_{\dot{\beta}}}$ may be combined into one term referred to as the damping-in-yaw derivative.

By considering the above assumptions, the lateral equations of motion are now written in the form used to analyze the data by the time-vector method.

Lateral force:

$$\frac{mV}{qS}\left(\frac{|\dot{\beta}|}{|\beta|} + \frac{|\dot{\psi}|}{|\beta|} - \alpha \frac{|\dot{\phi}|}{|\beta|}\right) - \frac{|C_Y|}{|\beta|} \frac{|\beta|}{|\beta|} = 0 \quad (9)$$

Rolling moment:

$$\frac{I_X}{qSb} \frac{|\ddot{\phi}|}{|\beta|} - \frac{I_{XZ}}{qSb} \frac{|\ddot{\psi}|}{|\beta|} - C_{l_\beta} \frac{|\beta|}{|\beta|} - C_{l_p} \frac{b}{2V} \frac{|\dot{\phi}|}{|\beta|} - C_{l_r} \frac{b}{2V} \frac{|\dot{\psi}|}{|\beta|} = 0 \quad (10)$$

Yawing moment:

$$\frac{I_Z}{qSb}\frac{|\ddot{\psi}|}{|\beta|} - \frac{I_{XZ}}{qSb}\frac{|\ddot{\phi}|}{|\beta|} - C_{n_\beta}\frac{|\beta|}{|\beta|} - C_{n_p}\frac{b}{2V}\frac{|\dot{\phi}|}{|\beta|} - \left(C_{n_r} - C_{n_{\dot{\beta}}}\right)\frac{b}{2V}\frac{|\dot{\psi}|}{|\beta|} = 0 \quad (11)$$

Notice that each of the equations was divided by β which is considered as the unit vector in the time-vector plots and the various amplitude ratios were determined from the data.

From preflight measurements, the mass, geometric, and inertia characteristics of the model were determined; from the radar, radiosonde, and telemeter-instrument system, the velocity, dynamic pressure, Mach number, lateral force, angle of attack, angle of sideslip, rolling angular acceleration, and yawing angular acceleration were obtained. Thus, the essential features of the short-period or Dutch-roll mode of the lateral motion were measured as a function of time and Mach number.

The following quantities were then determined from the measurements: period, damping factor, undamped natural circular frequency, lateral-force coefficient, time lag between sideslip angle and rolling angular acceleration, and the amplitude ratios of rolling angular acceleration tc sideslip angle and lateral force to sideslip angle. An attempt was made to determine the amplitude ratio of yawing angular acceleration to sideslip angle, but this was not possible because of the erratic readings of the transverse accelerometer in the nose of the model. These erratic readings were due to the model experiencing both random and regular high-frequency oscillations superimposed upon the short-period oscillatiens in such a manner that the readings of this instrument were unreliable.

The solution of the lateral equations of motion (eqs. 9 to 11) by use of the time-vector method to determine the lateral stability derivatives is illustrated in figure 7 for the lateral oscillations following a rudder impulse at $M \approx 1.10$. The lateral-force equation was solved first (see fig. 7(a)) to obtain the yawing angular velocity. The displacement vector amplitude $\frac{|\beta|}{|\beta|}$ was plotted to the right with magnitude equal to unity in order to determine the scale of the vector polygon. The phase angle was considered to be 0°. The first vector plotted was the $\frac{mV}{qS}\frac{|\dot{\beta}|}{|\beta|}$ vector where the amplitude ratio $\frac{|\dot{\beta}|}{|\beta|}$ was determined by multiplying the unit vector $\frac{|\beta|}{|\beta|}$ by the undamped natural circular frequency $(\omega^2 + a^2)^{1/2}$, and the phase angle $\Phi_{\dot{\beta}\beta}$ was determined from the damping angle $\left(90^\circ + \tan^{-1}\frac{a}{\omega}\right)$. See equation 4. This vector was plotted

in the positive direction of $\dot{\beta}$. To this vector was added the $-\frac{|C_Y|}{|\beta|}\frac{|\beta|}{|\beta|}$ vector and, since $\frac{|C_Y|}{|\beta|}$ is negative, it is plotted in the positive β direction. The vector $-\frac{mV}{qS}\alpha\frac{|\dot{\phi}|}{|\beta|}$ was added next, where the amplitude ratio $\frac{|\dot{\phi}|}{|\beta|}$ was determined from the measured amplitude ratio $\frac{|\ddot{\phi}|}{|\beta|}$ by dividing $\frac{|\ddot{\phi}|}{|\beta|}$ by the undamped natural circular frequency, and the phase angle $\Phi_{\dot{\phi}\ddot{\phi}}$ was determined from the damping angle $\left(90^\circ + \tan^{-1}\frac{a}{\omega}\right)$. Note for this configuration since α is negative the vector $-\frac{mV}{qS}\alpha\frac{|\dot{\phi}|}{|\beta|}$ is plotted in the positive direction of $\dot{\phi}$. The vector length now required to close the vector polygon is the amplitude ratio $\frac{mV}{qS}\frac{|\dot{\psi}|}{|\beta|}$ and the phase angle $\Phi_{\dot{\psi}\beta}$ is the angle measured between the $\dot{\psi}$ vector and the β vector. Inasmuch as the yawing angular velocity was known, the yawing angular acceleration was determined by use of the basic properties of time vectors.

After these quantities have been determined, either the rolling-moment or yawing-moment equation may be solved in a manner similar to the lateral-force equation. In both of these equations, the inertia vectors are known completely, whereas the aerodynamic vectors are known only in direction, so that two of these aerodynamic vectors must be solved for as a function of the third. Generally, it is best to estimate the amplitude of the smallest vector so that greater accuracy is allowed and then determine the other two by closing the vector polygon. However, transonic wind-tunnel values of C_{l_p} are available for this configuration from reference 9; thus, values of C_{l_r} and C_{l_β} were determined from the vector solution of the rolling-moment equation. (See fig. 7(b).) Values of $\left(C_{n_r} - C_{n_{\dot{\beta}}}\right)$, plotted in $\dot{\psi}$ direction, and C_{n_β} were determined from the vector solution of the yawing-moment equation as functions of C_{n_p}. (See fig. 7(c).) Values of C_{n_p} were assumed to be -0.10, 0, and 0.10, and values of C_{n_β} and $\left(C_{n_r} - C_{n_{\dot{\beta}}}\right)$

were determined for each of these values of C_{n_p} in order to show that C_{n_β} and $\left(C_{n_r} - C_{n_{\dot{\beta}}}\right)$ are linearly dependent upon C_{n_p} in the vector plots. It is seen from figure 7(c) that C_{n_p} has little effect on C_{n_β} whereas it greatly affects $C_{n_r} - C_{n_{\dot{\beta}}}$. The variation of C_{n_β} with Mach number shown later in the paper is presented for $C_{n_p} = 0$, whereas the variation of $C_{n_r} - C_{n_{\dot{\beta}}}$ with Mach number is presented for all three values of C_{n_p}.

RESULTS AND DISCUSSION

Time History

A portion of the time history of the lateral motions experienced by the model due to a yaw disturbance caused by an impulsive deflection of the rudder is shown in figure 8 where the variation with time of the rudder deflection, rolling angular acceleration, lateral-force coefficient, angle of sideslip, and angle of attack are presented. The appearance of the oscillations is that of a lightly damped sinusoid.

Although the model was disturbed essentially in yaw, an induced pitching motion was recorded. It is believed that this angle-of-attack change is small enough to have a negligible effect on the lateral motions. The possible effects of inertia coupling experienced by some rocket-propelled models (see, for example, ref. 10) have been checked for this configuration and the effects were found to be small.

From the time history of the lateral motions of the model, the general characteristics of the Dutch-roll oscillation were determined. These characteristics are shown in figure 9 where the period, total damping factor, and undamped natural circular frequency are presented. Note that the period and the undamped natural circular frequency show the usual variation with Mach number, that is, decreasing and increasing, respectively, with increasing Mach number whereas the total damping factor is low throughout the Mach number range of the tests and near $M = 0.95$ it is unstable. The period and total damping factor were determined from the oscillations in sideslip angle, lateral-force coefficient, and rolling angular acceleration, and the undamped natural circular frequency was determined from the faired variation of the period and total damping factor with Mach number.

Trim Characteristics

The variations of the model trim characteristics with Mach number shown in figure 10 as trim sideslip angle, trim lateral-force coefficient, and trim angle of attack. There were no abrupt trim changes; however, the model changed trim somewhat throughout the test Mach number range. The trim change experienced in angle of attack was similar to the trim angle-of-attack variation reported in reference 1. The trim normal-force coefficient varied from 0.04 at $M = 0.88$ to 0.05 at $M = 1.1$.

Amplitude Ratio and Phase of Rolling Angular Acceleration to Angle of Sideslip

The variation with Mach number of the amplitude ratio and phase of rolling angular acceleration to angle of sideslip due to a yaw disturbance is shown in figure 11. It is important to note that these dynamic characteristics are for the model and the full-scale airplane may or may not have the same phase or amplitude ratio since the mass and inertia characteristics of an airplane and a model would be considerably different.

Sideslip Derivatives

Cross plots.- A typical cross plot showing the variation of lateral-force coefficient with angle of sideslip is shown in figure 12. Note that, although the model was symmetrical and the rudder did not float when undeflected, zero lateral force did not occur at zero angle of sideslip. This could be possibly due to an instrument shift during the flight. Since there was very little scatter in the data points from the faired variation of C_Y against β and very little hysteresis throughout the Mach number range of the test, it is felt that the sum of the derivatives C_{Y_p} and C_{Y_r} is zero.

Lateral-force derivative.- From the cross plots of C_Y against β the lateral-force derivative C_{Y_β} was determined and the variation of C_{Y_β} with Mach number is shown in figure 13(a). This variation is similar to the variation of the slope of the lift curve for wings having moderate aspect ratio, low sweep, and thick airfoil sections; thus, the main contribution to C_{Y_β} is the vertical tail. Furthermore, it is believed that the high value of C_{Y_β} near $M = 1.0$ is greatly due to the induced

sidewash across the vertical tail. Tail-on and tail-off data at low and high speeds indicate a favorable induced sidewash effect and it is believed that the high value of C_{Y_β} near $M = 1.0$ measured in the present test could be due to this favorable sidewash effect but of larger magnitude.

Directional stability derivative.- The variation of the directional stability derivative C_{n_β} with Mach number as determined from the results of the vector analysis is shown in figure 13(b). The data are presented for $C_{n_p} = 0$ as explained in the analysis section and indicate generally an increase in C_{n_β} with increasing Mach number. Calculation of the isolated tail contribution to C_{n_β} based on the C_{Y_β} data of figure 13(a) indicates that the isolated tail contribution is considerably greater than the data of figure 13(b) throughout the Mach number range of this test. It is believed then that the wing-body contribution to C_{n_β} is destabilizing and of rather large magnitude. Also shown in figure 13(b) is a comparison of C_{n_β} as determined from the single-degree-of-freedom method. (See ref. 11). The single-degree-of-freedom method neglects the product-of-inertia term and assumes $C_{n_p} = 0$ in the yawing-moment equation; thus, C_{n_β} is determined directly from the period of the yawing oscillation. Note that the agreement between C_{n_β} as determined from the vector analysis and the single-degree-of-freedom method is good. This result is due to assuming $C_{n_p} = 0$ in the vector analysis and also due to the fact that for this configuration the product of inertia is very small. It appears then that for configurations for which the product of inertia is very small and for which C_{n_p} is nearly equal to zero, the single-degree-of-freedom method allows the determination of C_{n_β} values that are good approximations to the actual values of C_{n_β}. These data then further substantiate the results obtained in reference 12. The C_{n_β} data of the present test determined from the single-degree-of-freedom method and the data of reference 1 do not show good agreement when these data are converted to the same center-of-gravity location. This result is primarily due to two reasons. The data of reference 1 were determined from rather random oscillations in yaw that were induced from pitching oscillations and also the moment of inertia in yaw of the model of reference 1 was estimated, not measured.

Effective dihedral derivative.- As discussed in the analysis section, values of the effective dihedral derivative C_{l_β} were determined from vector analysis by knowing values of the damping-in-roll derivative C_{l_p}. The variation of C_{l_β} with Mach number is shown in figure 13(c) for the low lift coefficients of this test. For completeness, the C_{l_p} data of reference 9 are included as figure 14. It is felt that the values of C_{l_β} shown in figure 13(c) are primarily due to the vertical tail and that wing-body interference effects almost cancel the contribution of the wing dihedral to C_{l_β}. Calculations of the isolated vertical-tail contribution to C_{l_β} tend to confirm this effect. Also high-speed wind-tunnel data indicate this effect; however, low-speed wind-tunnel data do not.

Moment Derivatives Due to Yawing

Rolling-moment-due-to-yawing derivative.- The variation of the rate of change of rolling-moment coefficient with yawing-angular-velocity factor C_{l_r} with Mach number is shown in figure 15(a). Values of C_{l_r} were determined from the vector analysis by knowing values of C_{l_p}, and data indicate that for the low lift coefficients of this test C_{l_r} is negative at $M = 0.9$ and increases positively with increasing Mach number to a large positive value at $M = 1.1$.

Damping-in-yaw derivative.- The variation of the damping-in-yaw derivative $C_{n_r} - C_{n_{\dot\beta}}$ with Mach number is shown in figure 15(b) where values of $C_{n_r} - C_{n_{\dot\beta}}$ are plotted for three values of C_{n_p}. These C_{n_p} values were chosen in such a way that they would cover a range of possible values for the configuration. As may be seen, $C_{n_r} - C_{n_{\dot\beta}}$ is linearly dependent upon C_{n_p}; thus, from the vector analysis, $C_{n_r} - C_{n_{\dot\beta}}$ may be obtained for any number of assumed values for C_{n_p}. The data plotted in figure 15(b) indicate that $C_{n_r} - C_{n_{\dot\beta}}$ is positive (unstable) over a small region of Mach number near $M = 0.95$; thus, possible dynamic instability of the Dutch-roll oscillation was indicated. Actually as shown in figure 9(b), dynamic instability was recorded in the time histories of the lateral motions over the same Mach number range. This instability may be due to separated flow on the thick vertical tail at these Mach

numbers. A comparison of the data in figure 15(b) with the total-damping-factor data in figure 9 indicates that for this configuration C_{n_p} is positive.

Another interesting point can be seen from figure 15(b). Since the total damping of the Dutch-roll oscillation is constant at any particular Mach number, increasing C_{n_p} positively results in values of $C_{n_r} - C_{n_{\dot{\beta}}}$ obtained from the vector diagrams that are less negative whereas decreasing C_{n_p} results in values of $C_{n_r} - C_{n_{\dot{\beta}}}$ that are more negative so that the beneficial contribution of positive values of C_{n_p} to the damping of the Dutch-roll oscillation becomes rather apparent. This effect is also shown in the vector plot of figure 7(c).

Comparison of Present Data With Other Data and With Estimates

Tests.- A comparison of the sideslip derivatives as obtained from the present test and the wind-tunnel tests of references 13 to 16 are shown in figure 16. Although there are rather large regions of Mach number where the sideslip-derivative data are not available, it is felt that the data from the present test together with the wind-tunnel test data may be used to determine faired variations of the sideslip derivatives with Mach number over the range of $M = 0.16$ to $M = 2.32$. It is also believed that the vector-analysis technique allows the determination of the sideslip derivatives to the same order of accuracy as does the wind-tunnel technique since data from two wind tunnels at almost the same Mach number show at least a 10-percent disagreement.

Estimates.- A comparison of the lateral-stability-derivative data of the present test and the estimated lateral stability derivatives for this configuration (ref. 17) is shown in figures 17 and 18.

The comparison of the sideslip derivatives is shown in figure 17. The differences between the values of C_{Y_β} may be attributed to much larger values of sidewash than were estimated whereas the differences between the values of C_{l_β} may be attributed to a stronger wing-fuselage interference effect than estimated. Estimated values of C_{n_β} taken from reference 17 were determined primarily from the test of reference 1 where C_{n_β} was determined from the single-degree-of-freedom method. The agreement between these data is good below $M = 0.95$ while the agreement at the higher Mach numbers is poor. As mentioned in a

previous section of this paper, the data of reference 1 were determined from random oscillations and an estimated moment of inertia in yaw so that the poor agreement in the C_{n_β} data may be due to this fact.

A comparison of the moment derivatives due to yawing is shown in figure 18 where the agreement is poor. The C_{l_r} data that were estimated do not show the abrupt variation with Mach number that the data of the present test indicate. The estimated values of C_{l_r} are for $\alpha = 0$ whereas the data for the present test are for angles of attack that vary from $\alpha = -1.2^\circ$ at $M = 0.9$ to $\alpha = -1.6^\circ$ at $M = 1.1$; however, it is felt that the poor agreement is not due to this difference in angle of attack, although it is possibly due to the method used to determine the estimated values. The differences in the damping-in-yaw data may be attributed to the fact that the $C_{n_{\dot\beta}}$ contribution was not estimated in reference 17.

Model High-Frequency and Random Oscillations

Throughout the flight the instrument telemeter system recorded high-frequency oscillations that were superimposed on the low-frequency Dutch-roll oscillations. A portion of the telemeter record showing these oscillations is presented in figure 19. The high-frequency oscillations were rather regular in nature from the peak Mach number of $M = 1.18$ to a Mach number of about $M = 0.96$ and had a frequency of about 90 cycles per second throughout this Mach number range. As stated in the preflight test section of this paper, shake tests were performed on the model. From these tests the first bending mode of the horizontal tail was determined to have a frequency of 86 cycles per second; however, the frequency of the vertical tail was not measured. The model of reference 1 did not experience these high-frequency oscillations and, since the only difference between the model of reference 1 and the model of the present test was in the construction of the tail sections (weaker for present test), it is believed that the model of the present test experienced flutter on some part of the empennage in the Mach number range from $M = 1.18$ to $M = 0.96$.

Below $M = 0.96$ the oscillations were random in nature; this condition is believed to indicate that the model experienced a form of buffet which may be explained as follows: The horizontal tail was mounted low on the vertical tail near the section of the fuselage incorporating a large boattail so that the region of the model bounded by the vertical tail, lower surface of the horizontal tail, and the fuselage represents a region where the static pressure may be considerably less than the free-stream static pressure and the flow may become unsteady. The results of reference 18 indicate that the static pressure in the region

discussed above should be about 0.5 of the free-stream static pressure from M = 1.0 to M = 0.9 and that a low-lift buffet is possible in the region of M = 0.99 to 0.87 because of the interference of the horizontal tail and body. It is believed then that the model experienced a low-lift buffet in the Mach number region below M = 0.95.

CONCLUSIONS

From the results of the flight test to determine the lateral stability characteristics of a rocket-propelled model of a supersonic airplane configuration employing a 40° sweptback wing having circular-arc sections, the following conclusions are indicated:

1. The time-vector method applied to the recorded Dutch-roll transient oscillations provided a useful method for the determination of the lateral stability derivatives. The results as obtained from the vector analysis indicate that, as the Mach number increases from 0.89 to 1.10, the directional stability and the effective dihedral increased, the damping in yaw was low and over a small region of Mach number was unstable, and the rate of change of rolling-moment coefficient with yawing-angular-velocity factor was negative at a Mach number of 0.89 and increased positively to a large positive value at a Mach number of 1.10.

2. The lateral-force derivative increased with increasing Mach number up to a Mach number of 0.98 and then decreased to the limit Mach number of the test.

3. For this configuration the lateral-force derivative was rather large, whereas the directional stability derivative was low; thus, a powerful sidewash effect on the vertical tail and a large wing-body destabilizing effect were indicated.

4. The model experienced an empennage flutter in the Mach number region above a Mach number of 0.96 and a low-lift buffet below M = 0.96.

Langley Aeronautical Laboratory,
National Advisory Committee for Aeronautics,
Langley Field, Va., January 17, 1954.

REFERENCES

1. D'Aiutolo, Charles T., and Mason, Homer P.: Preliminary Results of the Flight Investigation Between Mach Numbers of 0.80 and 1.36 of a Rocket-Powered Model of a Supersonic Airplane Configuration Having a Tapered Wing With Circular-Arc Sections and 40° Sweepback. NACA RM L50H29a, 1950.

2. Mitchell, Jesse L., and Peck, Robert F.: Investigation of the Lateral Stability Characteristics of the Douglas X-3 Configuration at Mach Numbers From 0.6 to 1.1 by Means of a Rocket-Propelled Model. NACA RM L54L20, 1955.

3. Mueller, R. K.: The Graphical Solution of Stability Problems. Jour. Aero. Sci., vol. 4, no. 8, June 1937, pp. 324-331.

4. Sternfield, L.: A Vector Method Approach to the Analysis of the Dynamic Lateral Stability of Aircraft. Jour. Aero. Sci., vol. 21, no. 4, Apr. 1954, pp. 251-256.

5. Larrabee, E. E.: Application of the Time Vector Method to the Analysis of Flight Test Lateral Oscillation Data. FRM No. 189, Cornell Aero. Lab. Inc., Sept. 9, 1953.

6. Breuhaus, W. O.: Resumé of the Time Vector Method as a Means for Analyzing Aircraft Stability Problems. WADC Tech. Rep. 52-299 (Contract No. AF33(038)-20659 RDO No. 461-1-2), Wright Air Dev. Center, U. S. Air Force, Nov. 1952.

7. Jones, B. Melvill: Dynamics of the Aeroplane. The Asymmetric or Lateral Moments. Vol V of Aerodynamic Theory, div. N, ch. III, secs. 10 and 21, W. F. Durand, Ed., Julius Springer (Berlin), 1935, pp. 61, 71-72.

8. Ikard, Wallace L.: An Air-Flow-Direction Pickup Suitable for Telemetering Use on Pilotless Airdraft. NACA RM L53K16, 1954.

9. Lockwood, Vernard E.: Damping-in-Roll Characteristics of a 42.7° Sweptback Wing as Determined From a Wind-Tunnel Investigation of a Twisted Semispan Wing. NACA RM L9F15, 1949.

10. Parks, James H.: Experimental Evidence of Sustained Coupled Longitudinal and Lateral Oscillations from a Rocket-Propelled Model of a 35° Swept Wing Airplane Configuration. NACA RM L54D15, 1954.

11. Bishop, Robert C., and Lomax, Harvard: A Simplified Method for Determining From Flight Data the Rate of Change of Yawing-Moment Coefficient With Sideslip. NACA TN 1076, 1946.

12. Purser, Paul E., and Mitchell, Jesse L.: Miscellaneous Directional-Stability Data for Several Airplane-Like Configurations From Rocket-Model Tests at Transonic Speeds. NACA RM L52E06b, 1952.

13. Goodson, Kenneth W., and Comisarow, Paul: Lateral Stability and Control Characteristics of an Airplane Model Having a 42.8° Sweptback Circular-Arc Wing With Aspect Ratio 4.00 and Taper Ratio 0.50, and Sweptback Tail Surfaces. NACA RM L7G31, 1947.

14. Spearman, M. Leroy: An Investigation of a Supersonic Aircraft Configuration Having a Tapered Wing With Circular-Arc Sections and 40° Sweepback - Static Lateral Stability Characteristics at Mach Numbers of 1.40 and 1.59. NACA RM L50C17, 1950.

15. Spearman, M. Leroy, and Palazzo, Edward B.: An Investigation of a Supersonic Aircraft Configuration Having a Tapered Wing With Circular-Arc Sections and 40° Sweepback - Static Longitudinal and Lateral Stability and Control Characteristics at a Mach Number of 1.89. NACA RM L54G26a, 1954.

16. Ellis, Macon C., Jr., Hasel, Lowell E., and Grigsby, Carl E.: Supersonic-Tunnel Tests of Two Supersonic Airplane Model Configurations. NACA RM L7J15, 1947.

17. Passman, R. A., and Meullen, N. F.: Revised Aerodynamic Parameters for the MX-743 (X-2) Airplane. Rep. No. 52-978-007, Bell Aircraft Corp., May 14, 1951.

18. Mason, Homer P.: Low-Lift Buffet Characteristics Obtained From Flight Tests of Unswept Thin Intersecting Surfaces and of Thick 35° Sweptback Surfaces. NACA RM L52H12, 1953.

TABLE I.- GEOMETRIC AND MASS CHARACTERISTICS OF THE MODEL

Wing:	
Total included area, sq ft	5.56
Aspect ratio	4
Sweep of quarter-chord line, deg	40
Taper ratio	0.5
Mean aerodynamic chord, ft	1.22
Airfoil sections normal to quarter-chord line (max. thickness at 0.50c)	10 percent circular arc
Horizontal tail:	
Total included area, sq ft	0.938
Aspect ratio	3.72
Sweep of quarter-chord line, deg	40
Taper ratio	0.5
Airfoil section parallel to fuselage reference line	NACA 65-008
Vertical tail:	
Area (exposed), sq ft	0.825
Aspect ratio (based on exposed area and span)	1.16
Sweepback of quarter chord, deg	33
Taper ratio	0.337
Mean aerodynamic chord, ft	1.02
Airfoil section, root	NACA 27-010
Airfoil section, tip	NACA 27-008
Fuselage:	
Fineness ratio (neglecting canopy and fairings)	9.58
Mass:	
Model weight, lb	190.5
Moment of inertia in yaw, I_Z, slug-ft^2	14.5
Moment of inertia in roll, I_X, slug-ft^2	4.0
Inclination of principal axes, ϵ, deg (down at nose)	4
Product of inertia, I_{XZ}, slug-ft^2	0.732
Center-of-gravity position, percent $\bar{c}$	20
Wing loading, lb/sq ft	34.2

TABLE II.- ESTIMATED ACCURACY OF BASIC QUANTITIES

[Values shown are positive or negative quantities]

Mach number	Accuracy of -											
	W, percent	I_Z, percent	I_X, percent	I_{XZ}, percent (a)	M, percent	q, percent	ω, percent	$\frac{\lvert\ddot{\phi}\rvert}{\lvert\beta\rvert}$, percent	$\frac{\lvert A_T/g\rvert}{\lvert\beta\rvert}$, percent	$\Phi\ddot{\phi}_\beta$, deg	α, deg	a, sec^{-1}
1.1	0.5	2.0	4.0	8.0	1.0	2.0	2.6	3.0	2.0	4	0.5	0.1
0.9	0.5	2.0	4.0	8.0	1.7	3.5	2.6	3.0	2.0	4	0.5	0.1

[a]This error is due primarily to estimated accuracy of inclination of principal axis, $\pm 0.5^\circ$.

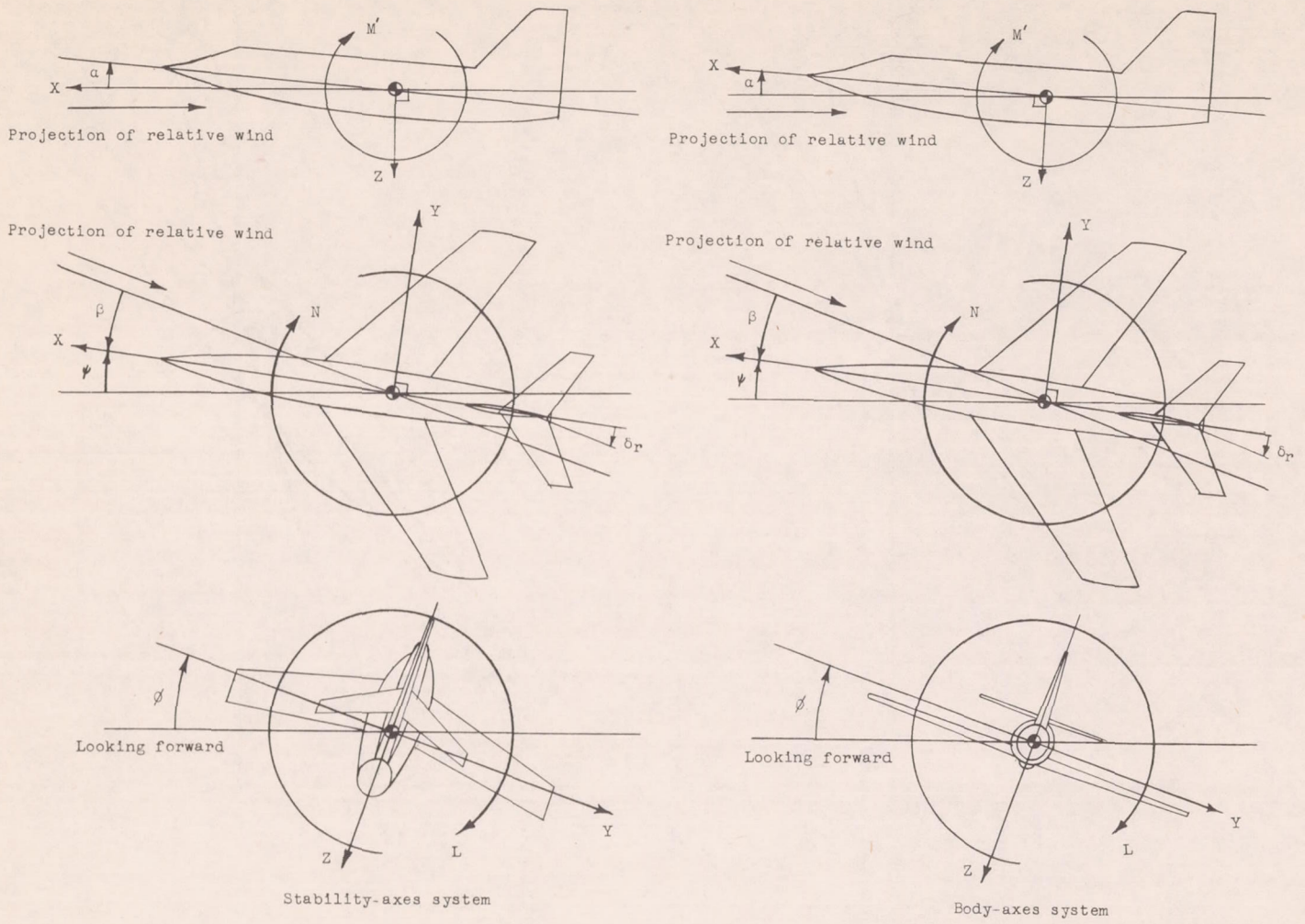


Figure 1.- Sketch showing stability- and body-axes system. Each view presents a plane of the axes system as viewed along the third axes. Arrows indicate positive direction of forces, moments, and angles.

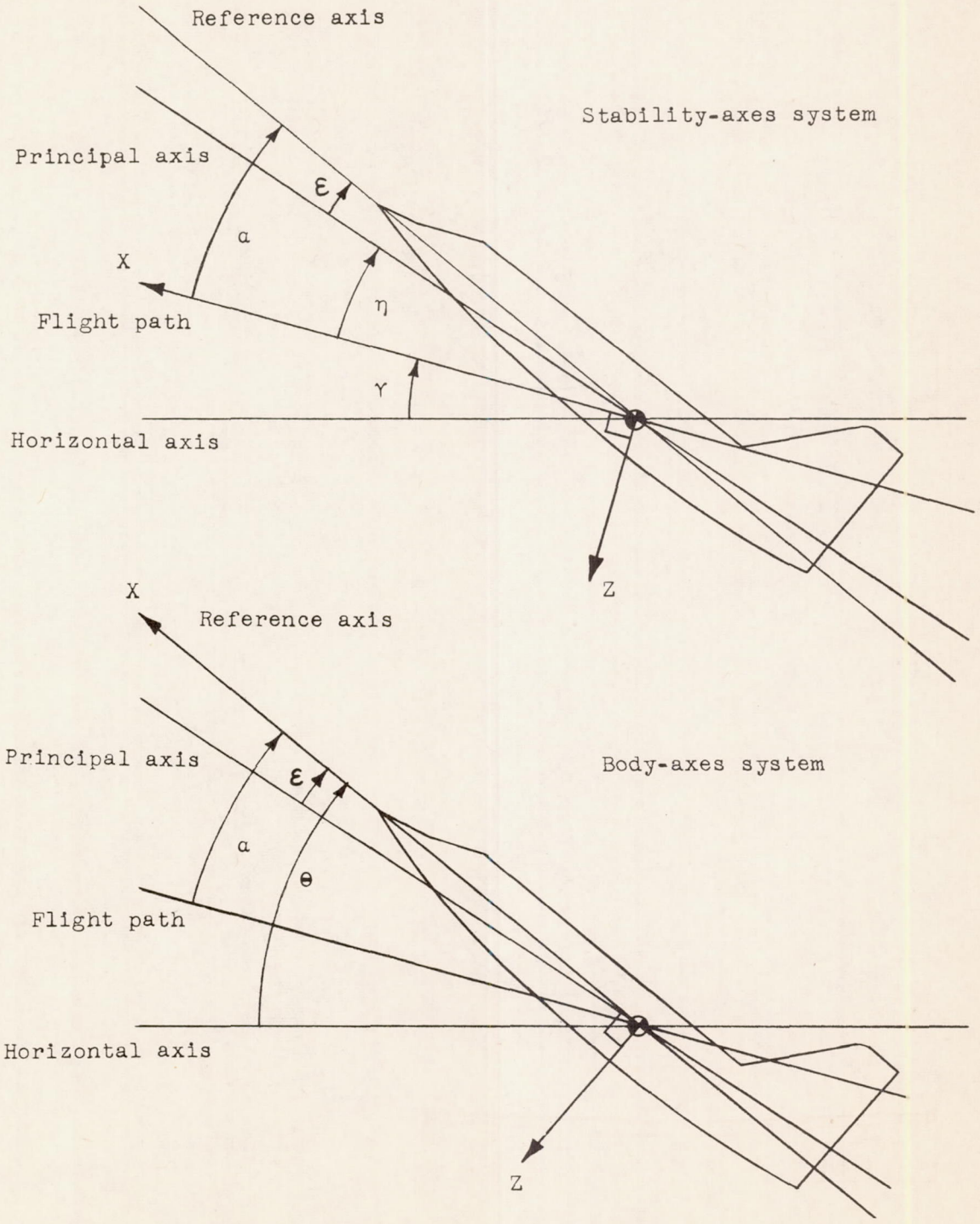
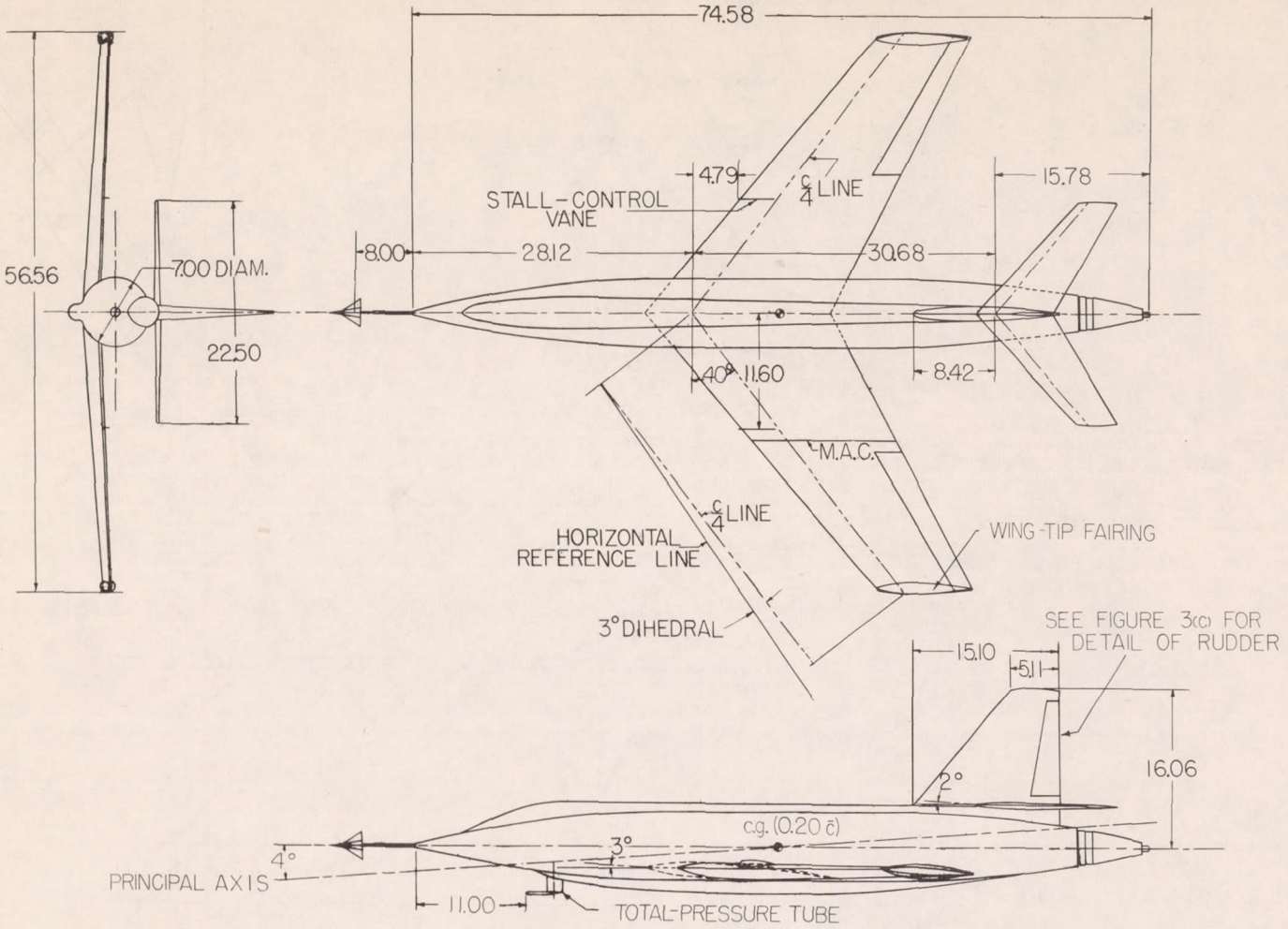
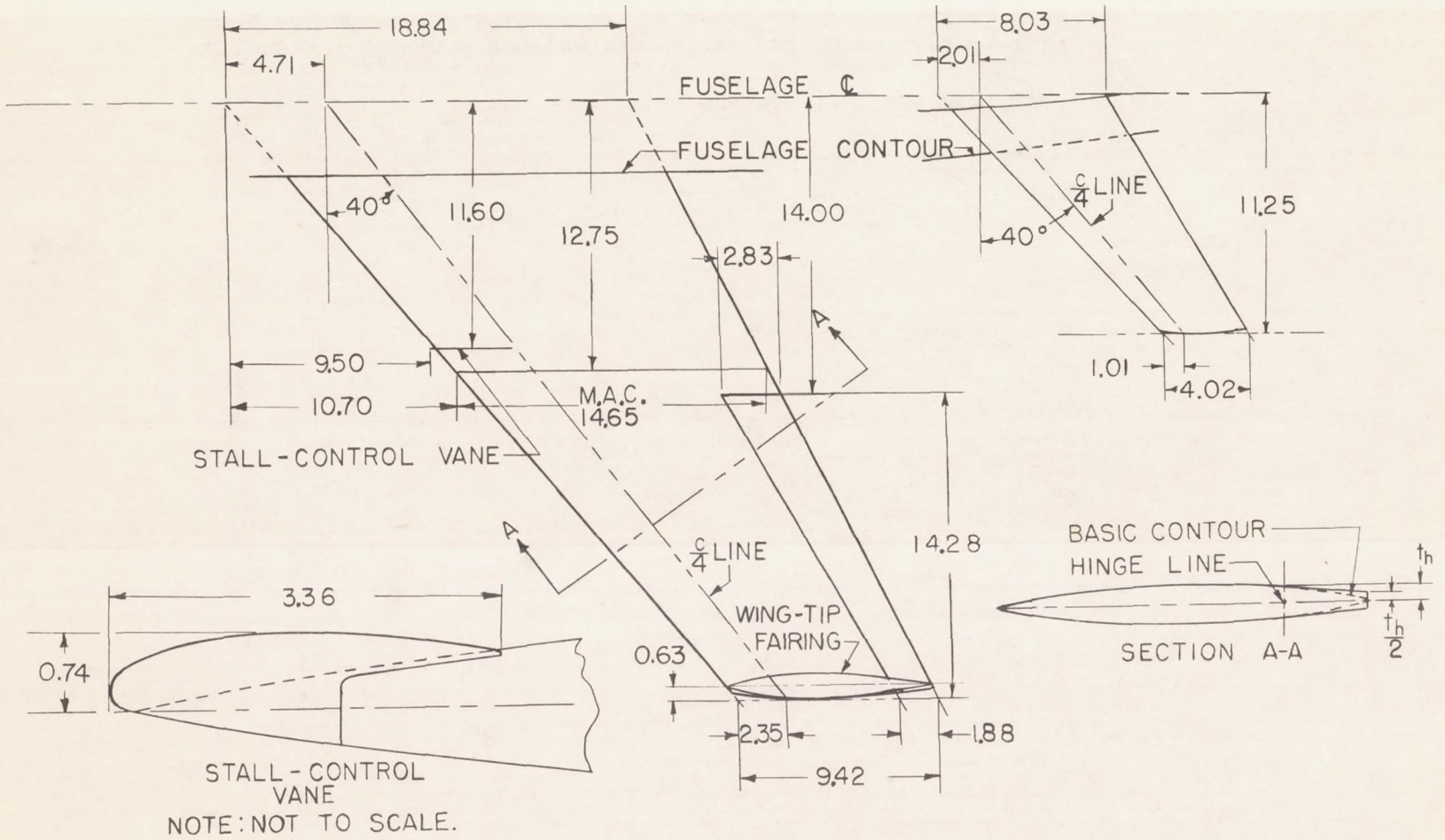


Figure 2.- Angular relationships in flight. Stability- and body-axes system. Arrows indicate positive direction of angles. $\eta = \alpha - \epsilon$.



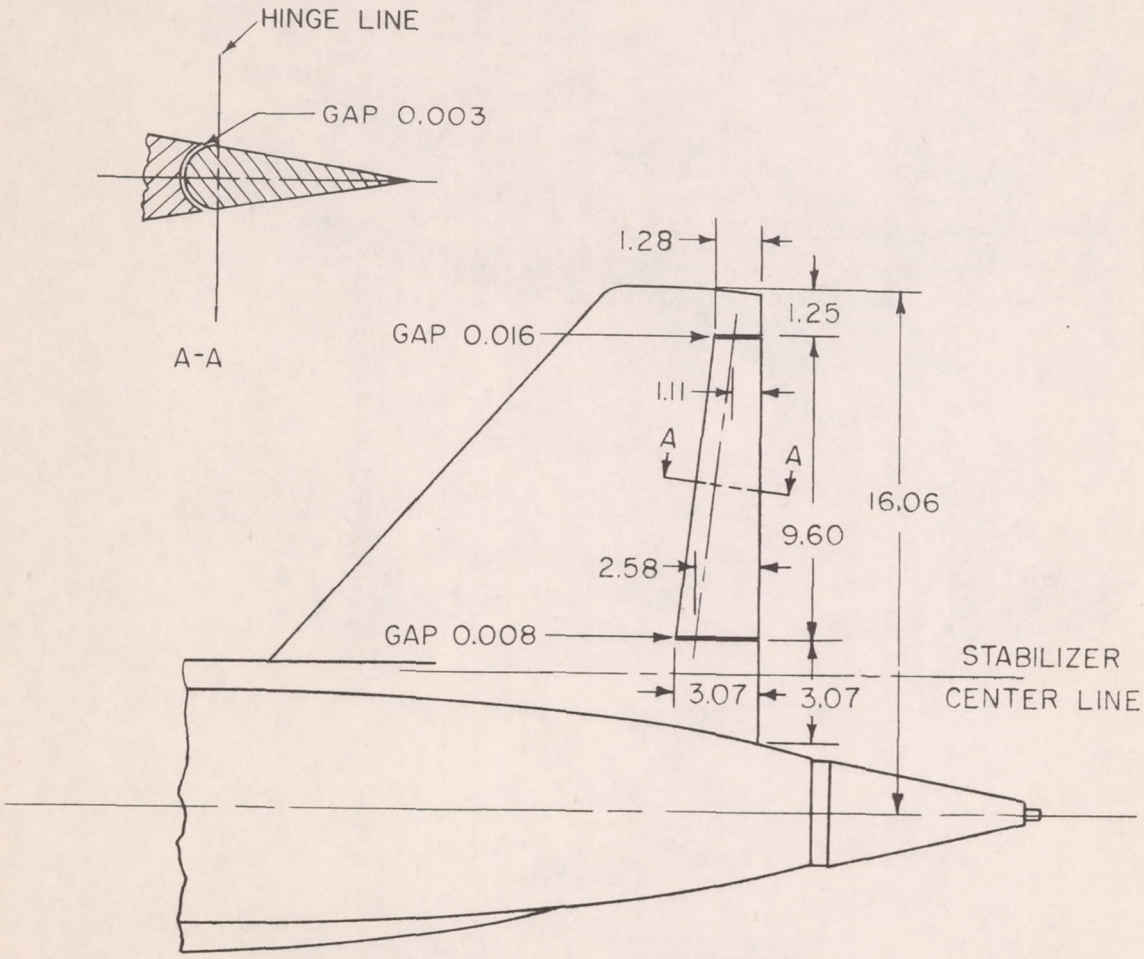
(a) General arrangement of supersonic airplane configuration.

Figure 3.- Drawings showing dimensions and characteristics of supersonic airplane configuration. All dimensions are in inches unless noted.



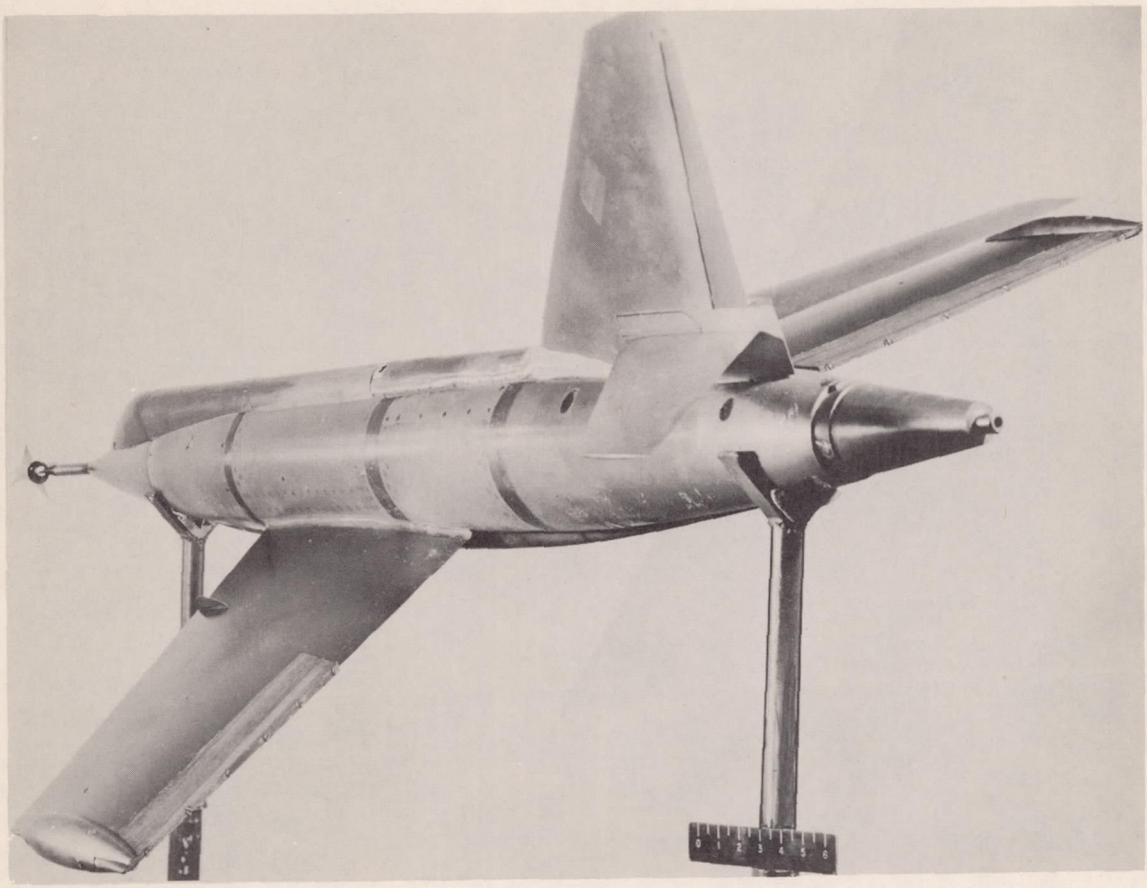
(b) Details of wing and horizontal stabilizer.

Figure 3.- Continued.

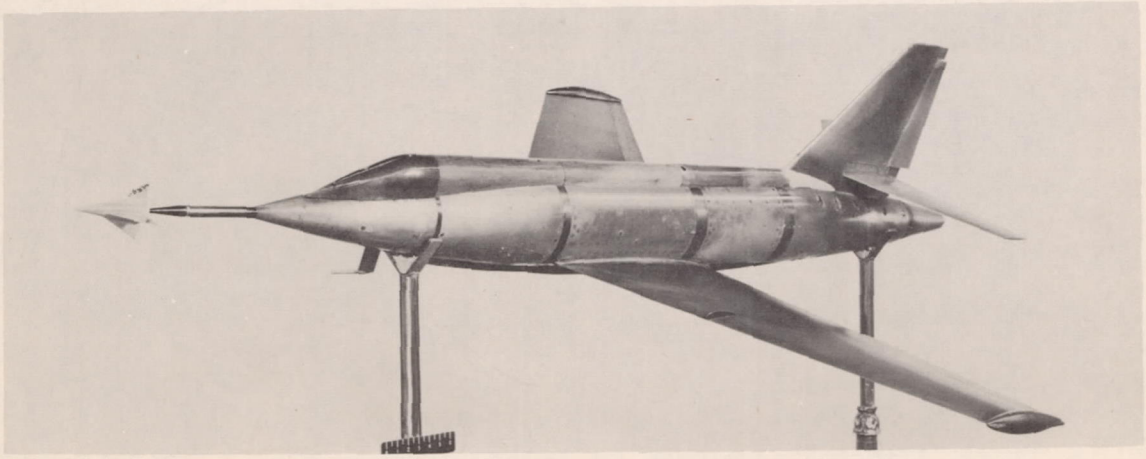


(c) Detail of rudder.

Figure 3.- Concluded.



(a) Three-quarter rear view. L-81369.1



(b) Three-quarter front view. L-81368.1

Figure 4.- Photographs of model of supersonic airplane configuration.



(c) Model-booster combination on launcher. L-82488.1

Figure 4.- Concluded.

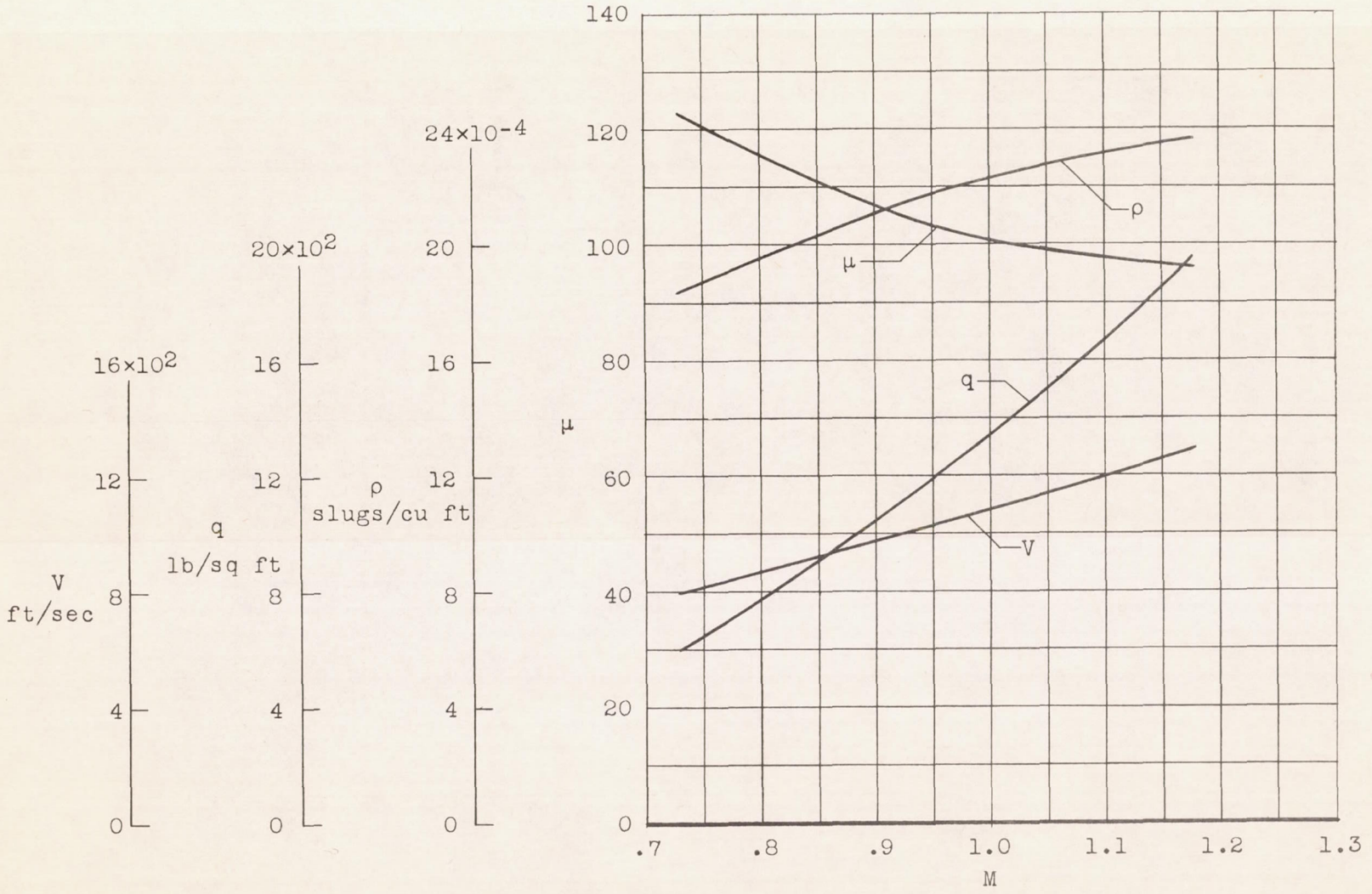


Figure 5.- Variation of velocity, dynamic pressure, air density, and relative density factor with Mach number.

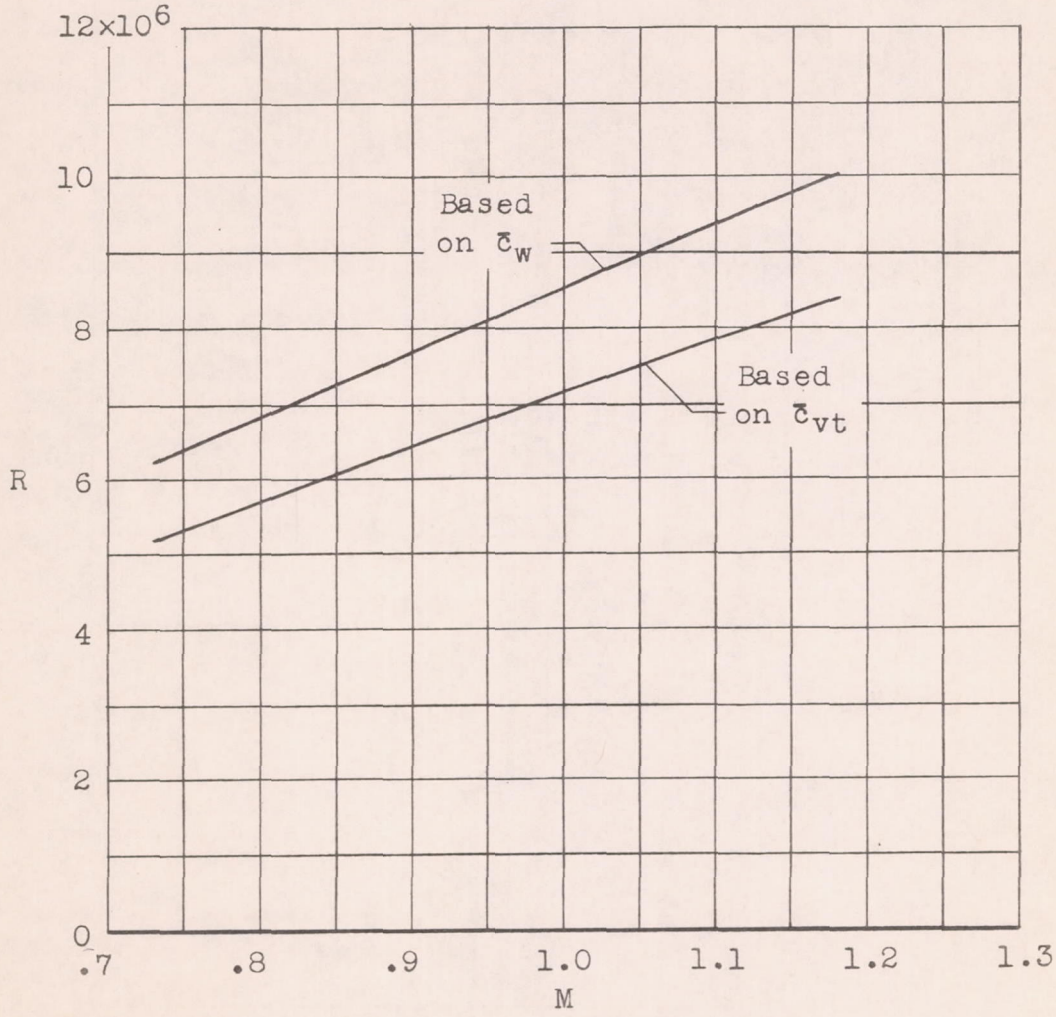
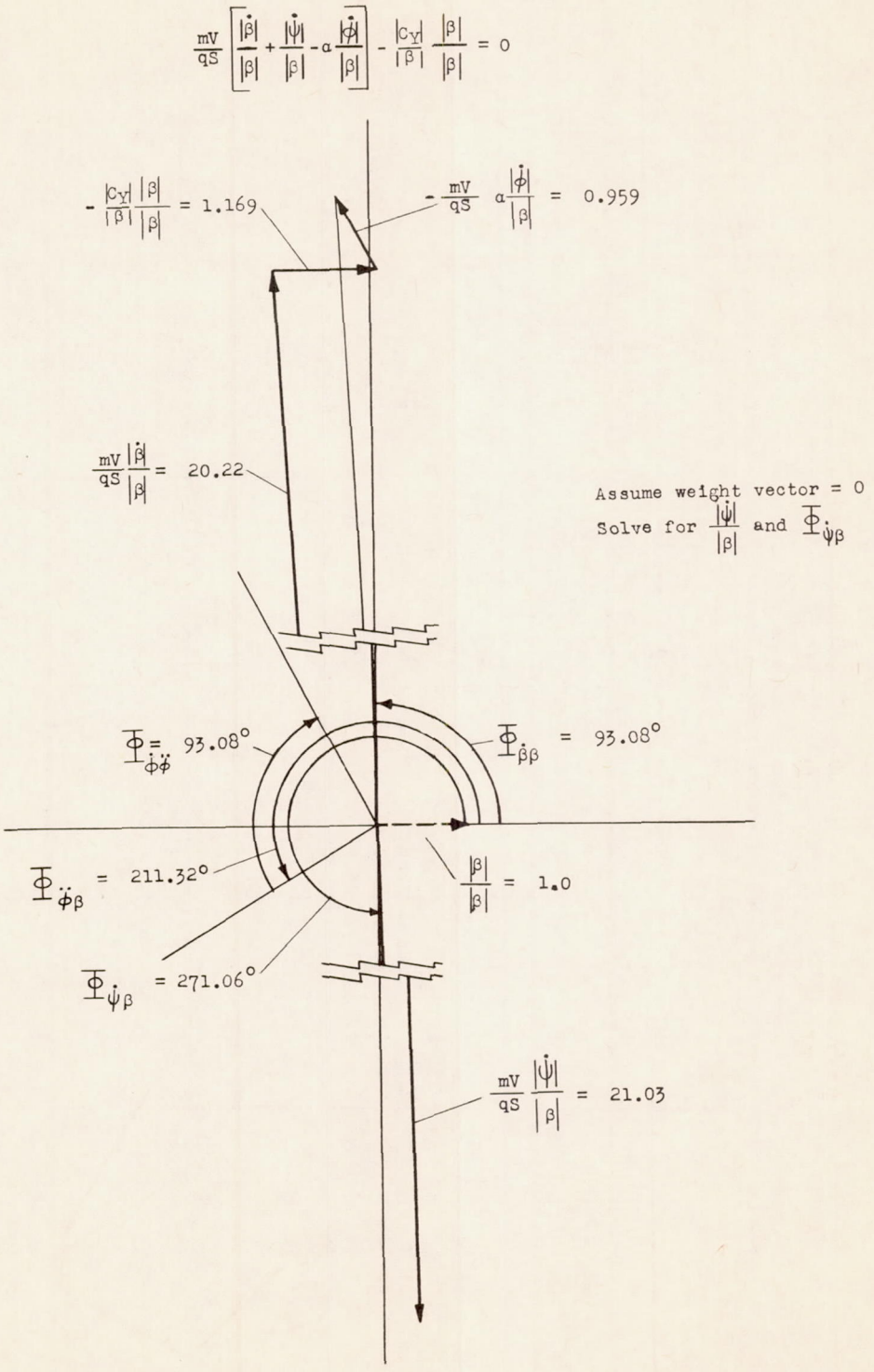
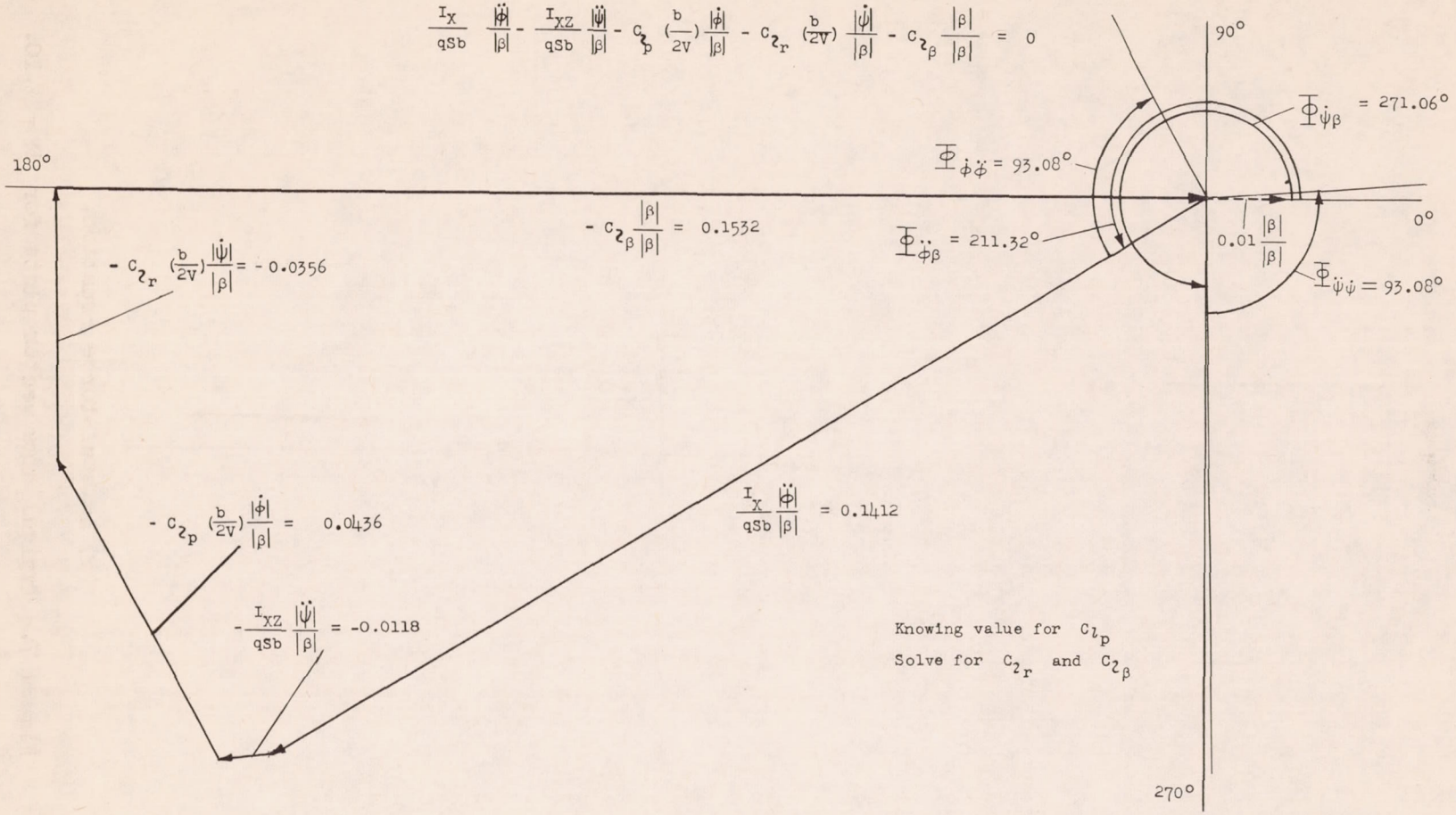


Figure 6.- Variation of Reynolds number with Mach number.



(a) Lateral-force equation.

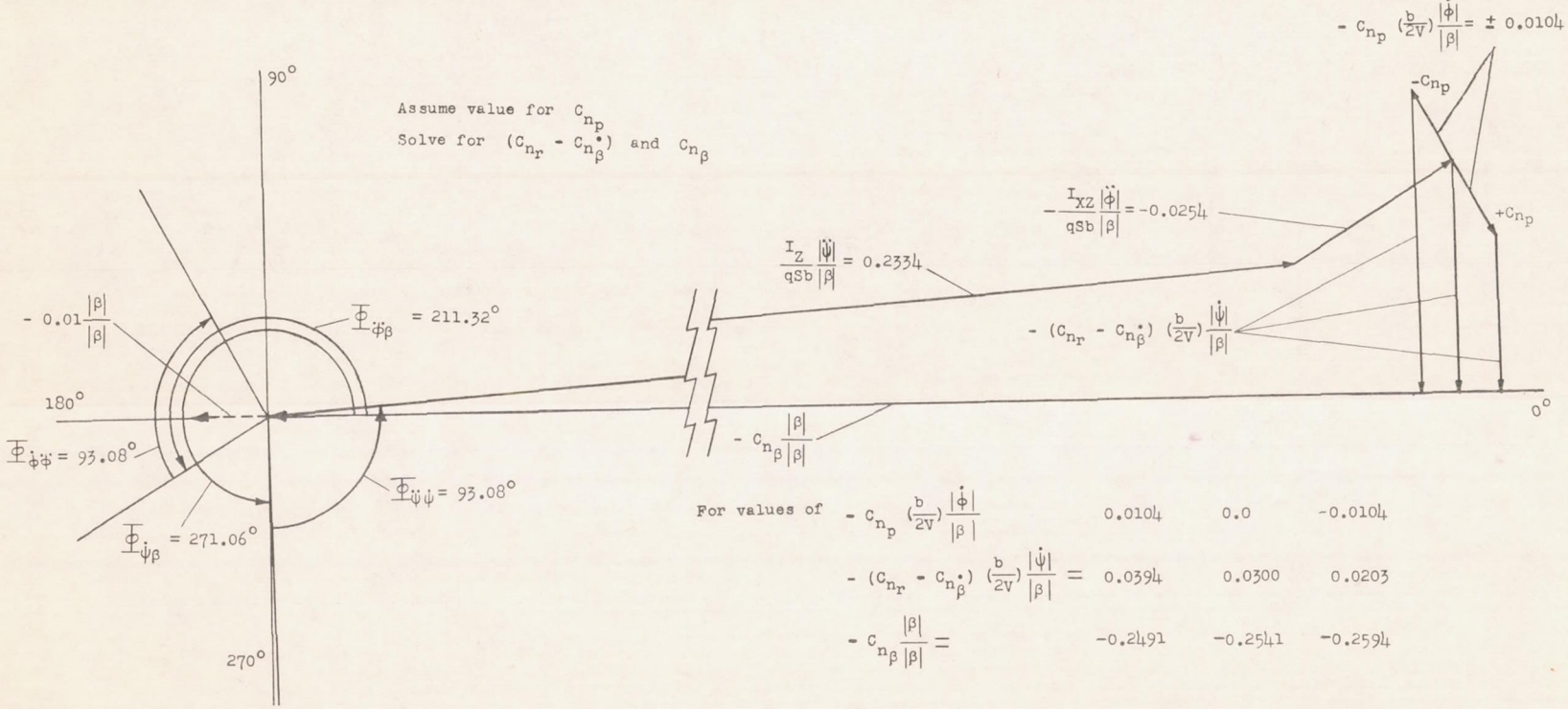
Figure 7.- Typical time vector plots for M = 1.10.



(b) Rolling-moment equation.

Figure 7.- Continued.

$$\frac{I_Z}{qSb}\frac{|\ddot{\psi}|}{|\beta|} - \frac{I_{XZ}}{qSb}\frac{|\ddot{\phi}|}{|\beta|} - C_{n_p}\left(\frac{b}{2V}\right)\frac{|\dot{\phi}|}{|\beta|} - \left(C_{n_r} - C_{n_{\dot{\beta}}}\right)\left(\frac{b}{2V}\right)\frac{|\dot{\psi}|}{|\beta|} - C_{n_\beta}\frac{|\beta|}{|\beta|} = 0$$



For values of $-C_{n_p}\left(\frac{b}{2V}\right)\frac{|\dot{\phi}|}{|\beta|}$ 0.0104 0.0 -0.0104

$-\left(C_{n_r} - C_{n_{\dot{\beta}}}\right)\left(\frac{b}{2V}\right)\frac{|\dot{\psi}|}{|\beta|} =$ 0.0394 0.0300 0.0203

$-C_{n_\beta}\frac{|\beta|}{|\beta|} =$ -0.2491 -0.2541 -0.2594

(c) Yawing-moment equation.

Figure 7.- Concluded.

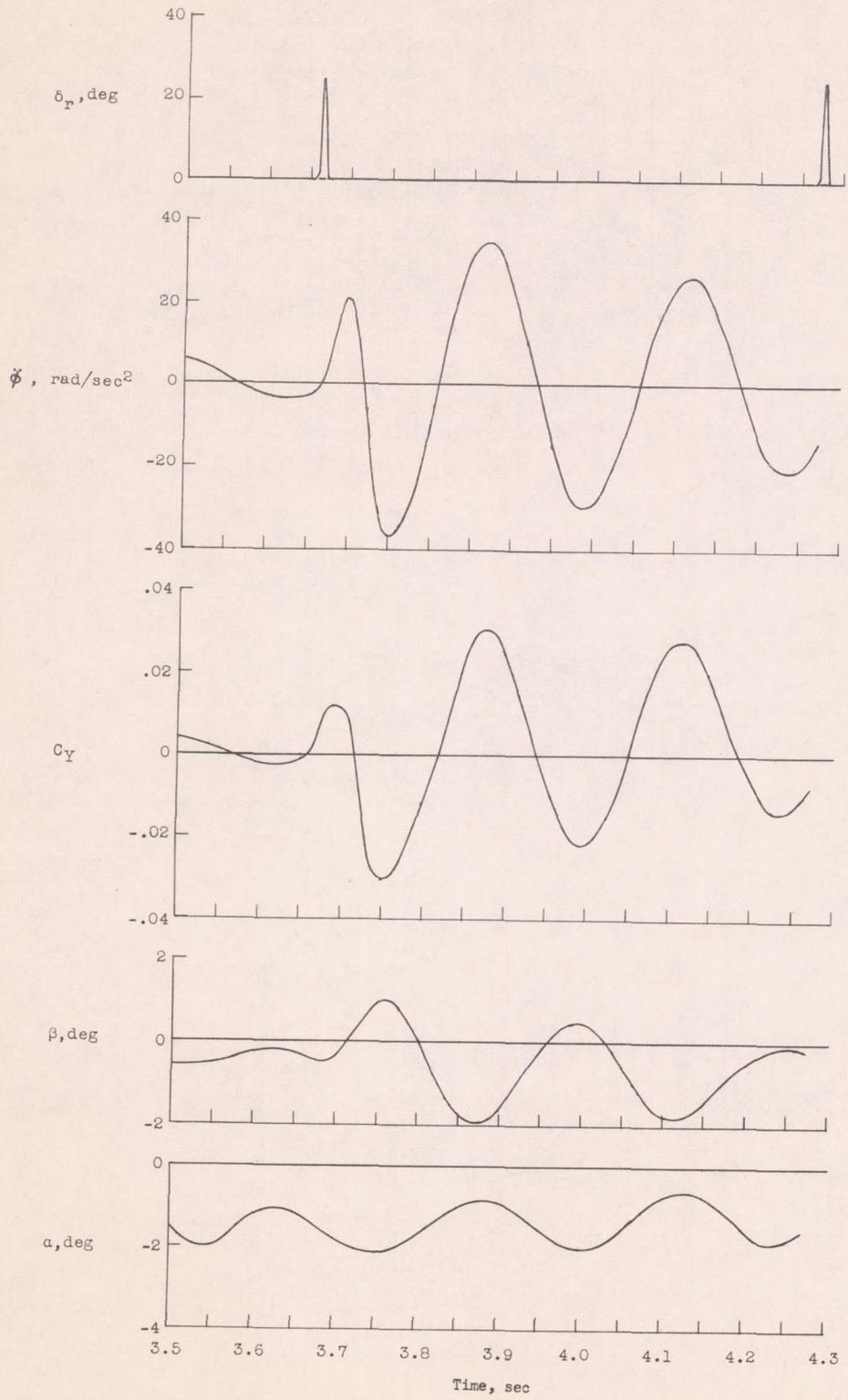
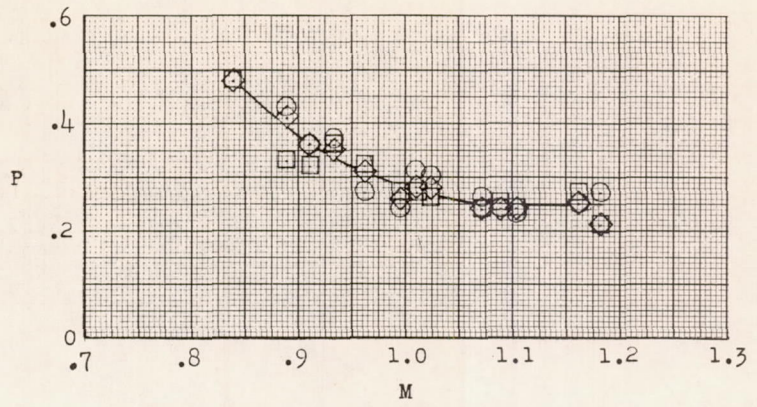
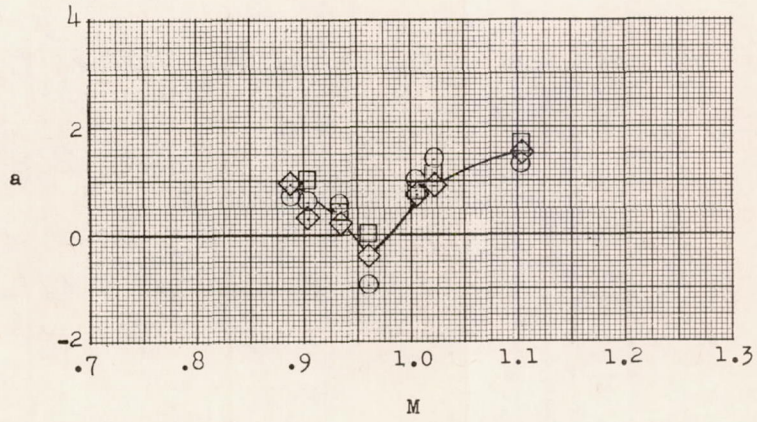


Figure 8.- Portion of time history of flight. M = 1.10.

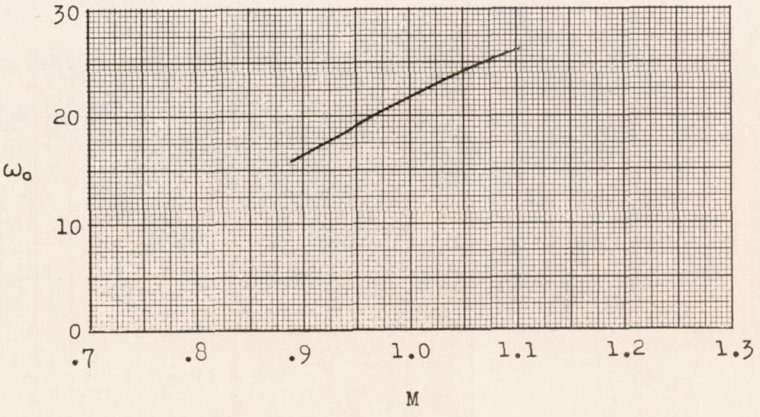


(a) Period of oscillations.

○ — β
□ — $\ddot{\Phi}$
◇ — C_Y



(b) Total damping factor.



(c) Undamped natural circular frequency.

Figure 9.- Variation of period of lateral oscillations, total damping factor, and undamped natural circular frequency with Mach number.

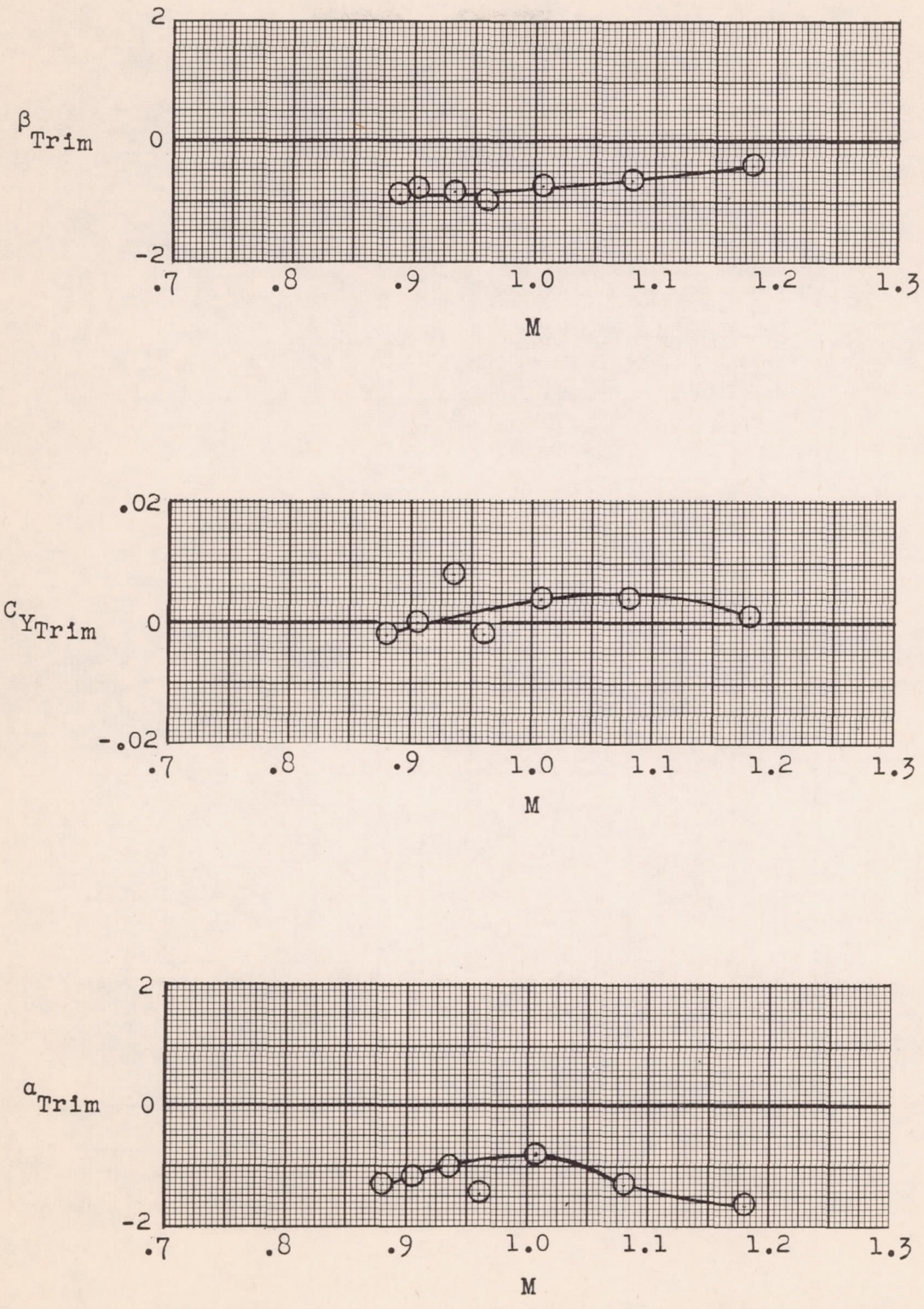
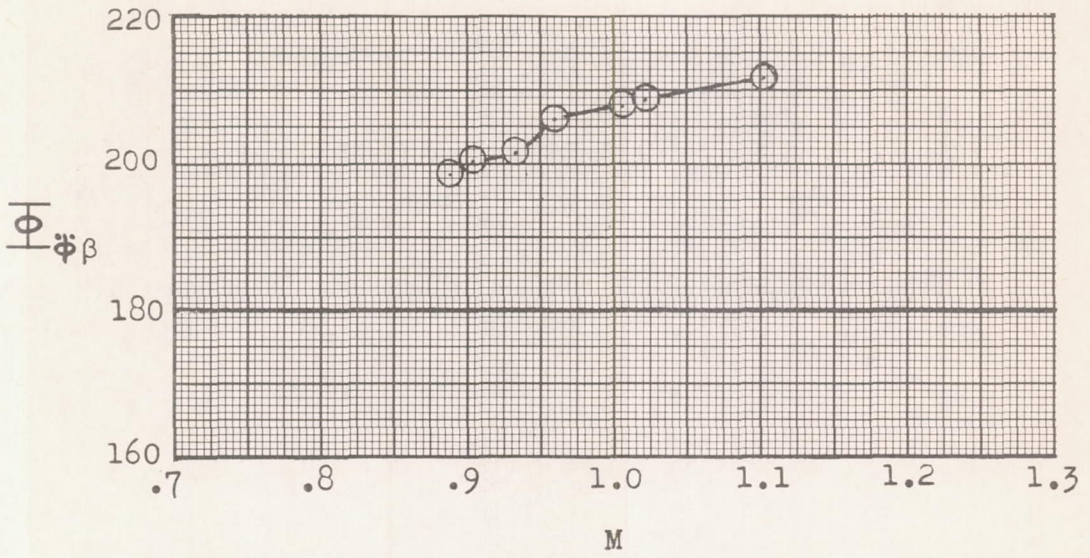


Figure 10.- Variation of trim characteristics with Mach number.



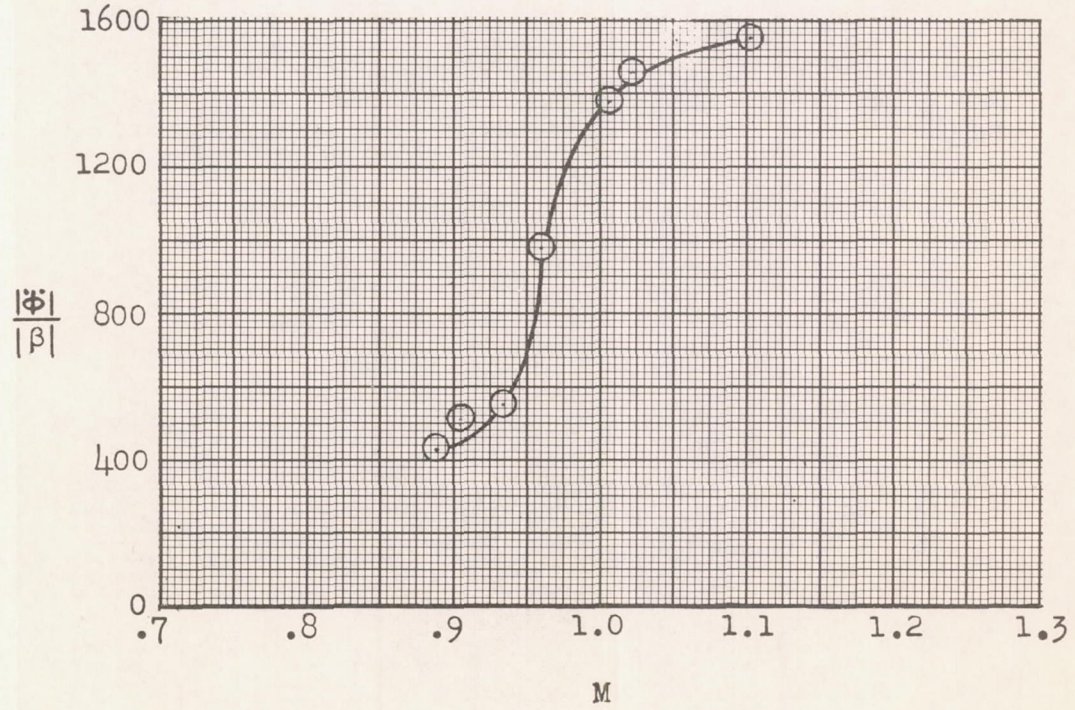


Figure 11.- Variation of amplitude ratio $\frac{|\ddot{\phi}|}{|\beta|}$ and phase angle $\Phi_{\ddot{\phi}\beta}$ with Mach number.

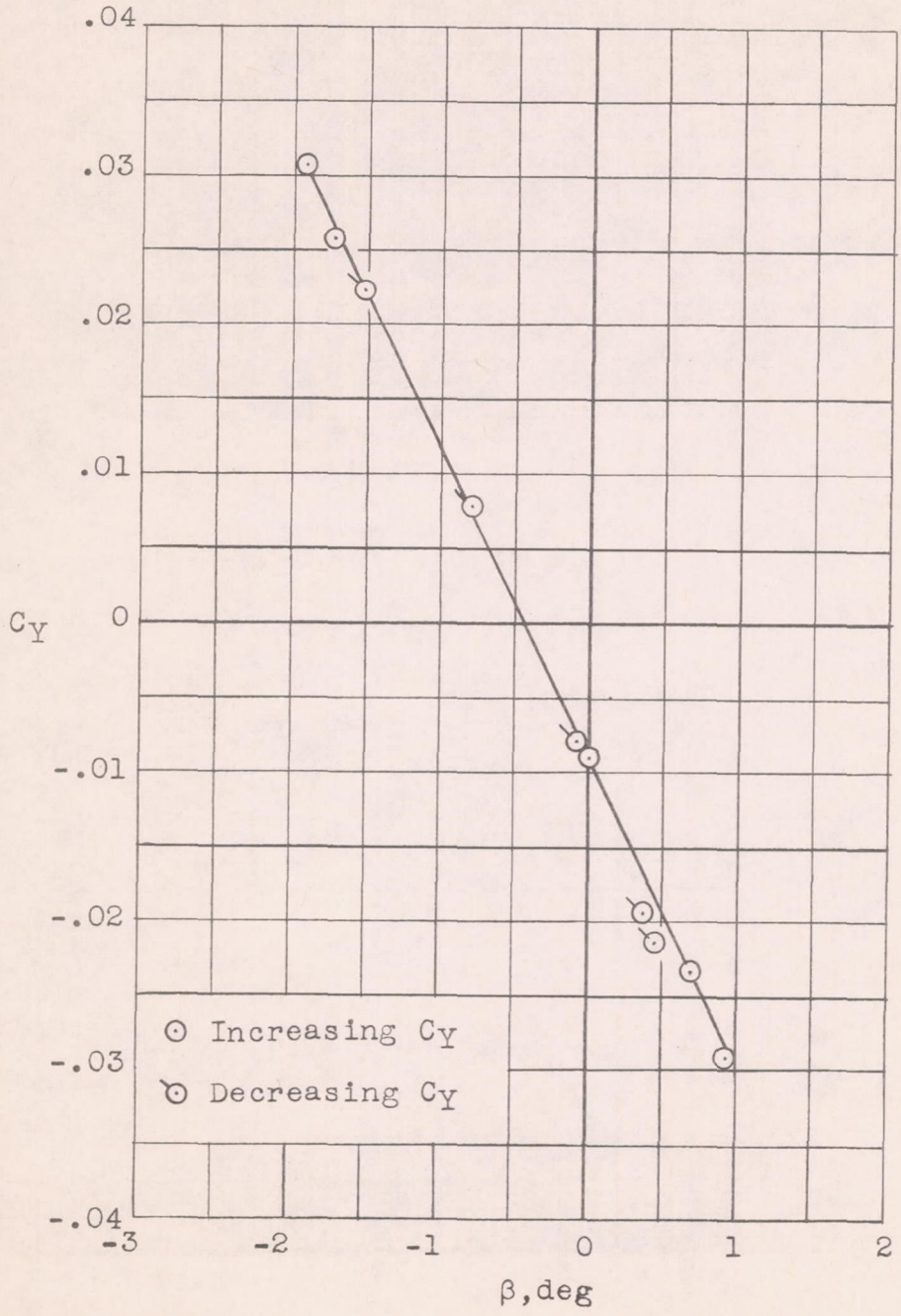
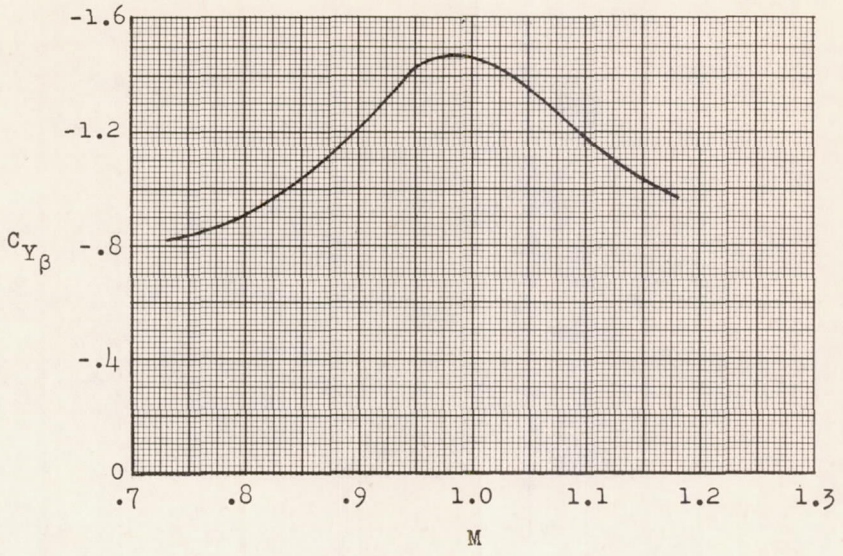
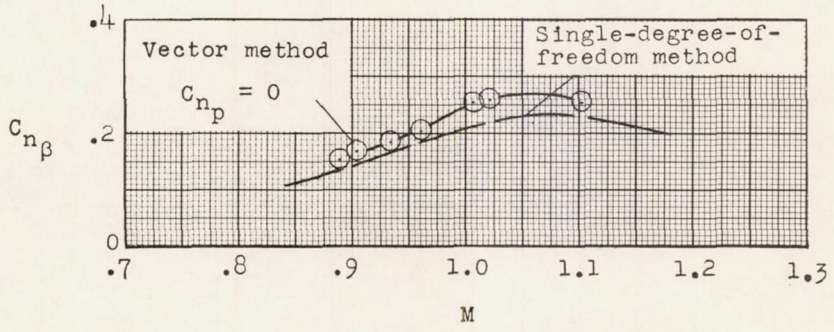


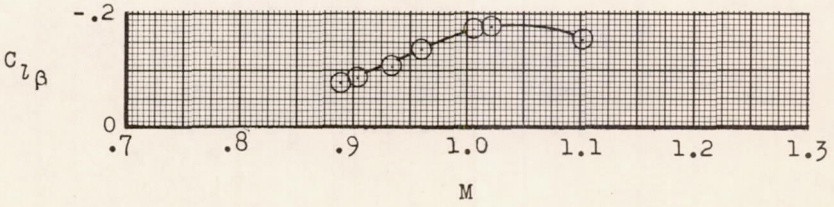
Figure 12.- Typical variation of lateral-force coefficient with sideslip angle at M = 1.10.



(a) Lateral-force derivative.



(b) Directional stability derivative.



(c) Effective dihedral derivative.

Figure 13.- Variation of sideslip derivatives with Mach number.

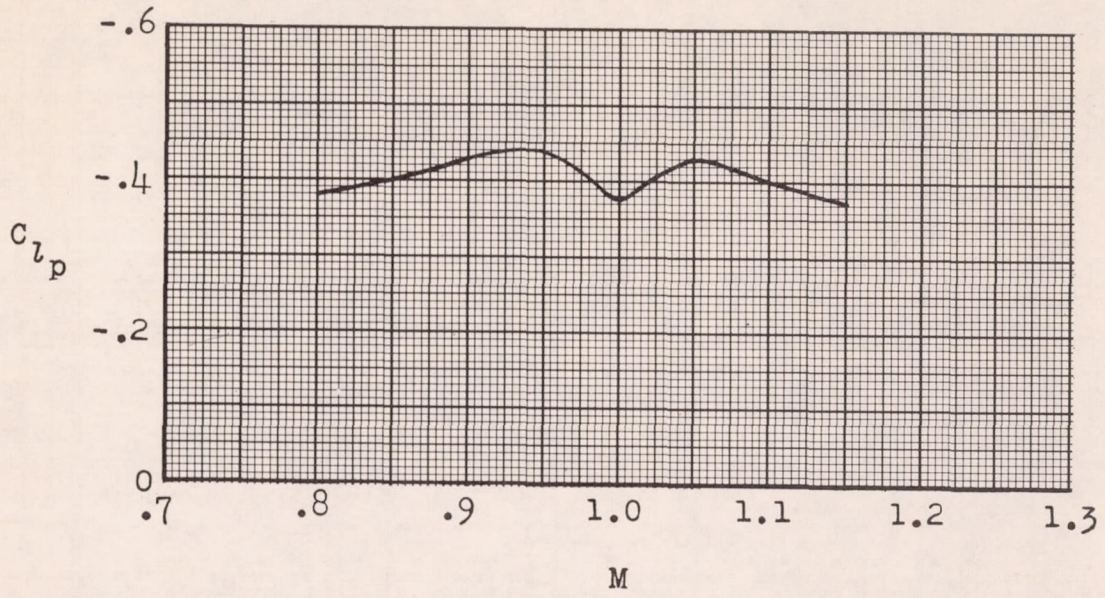
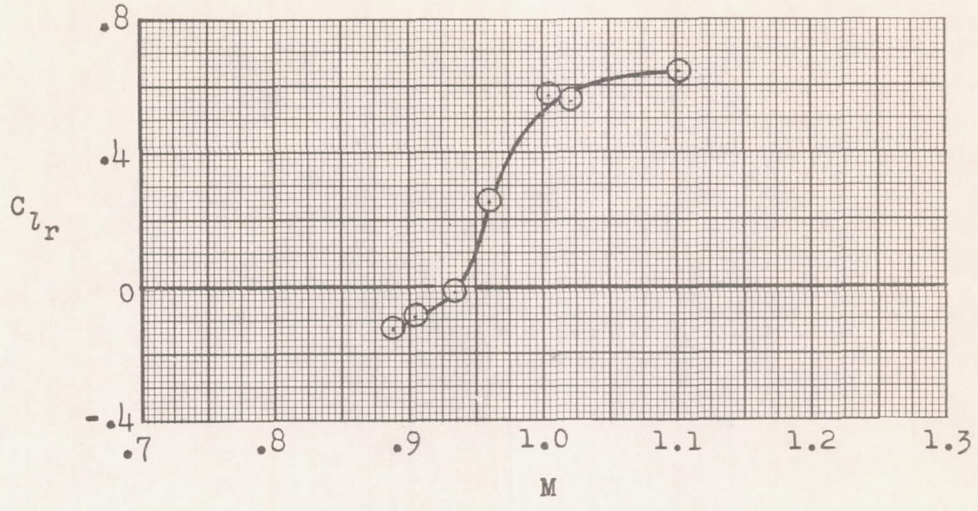


Figure 14.- Variation of damping-in-roll derivative with Mach number as obtained from reference 9.



(a) Rolling-moment-due-to-yawing derivative.



(b) Damping-in-yaw derivative.

Figure 15.- Variation of moment derivatives due to yawing with Mach number.

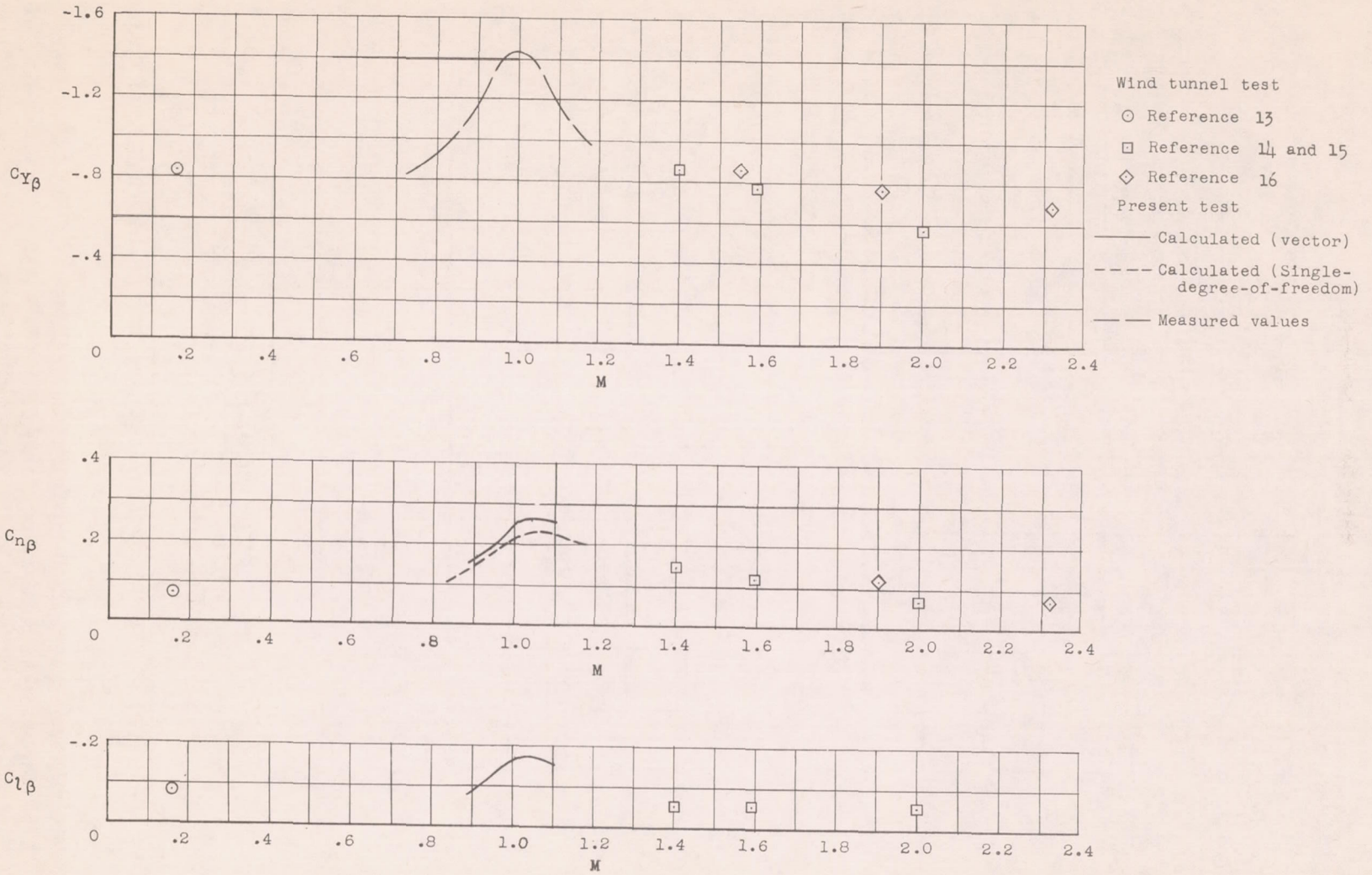


Figure 16.- Comparison of sideslip stability derivatives from various tests.

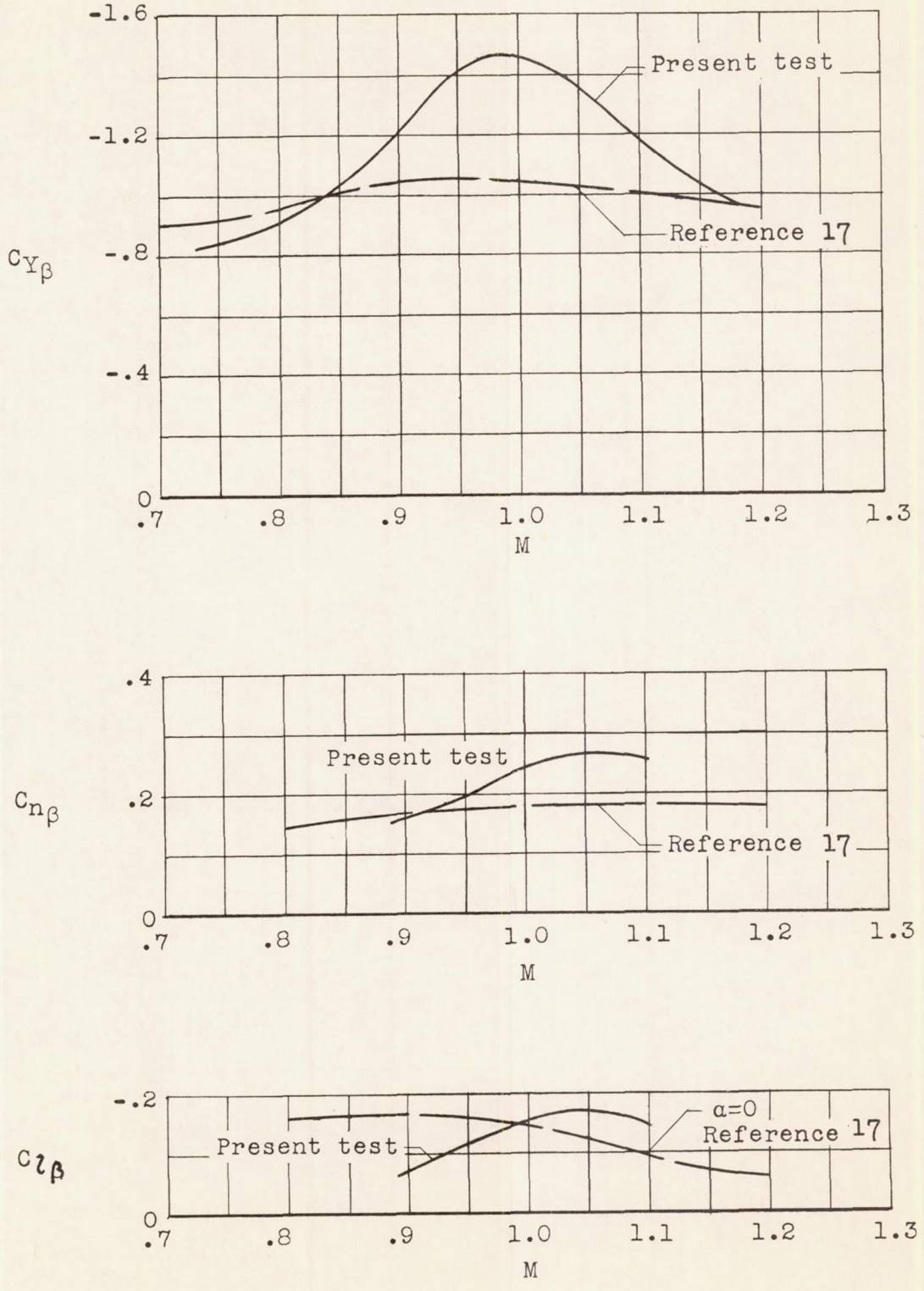
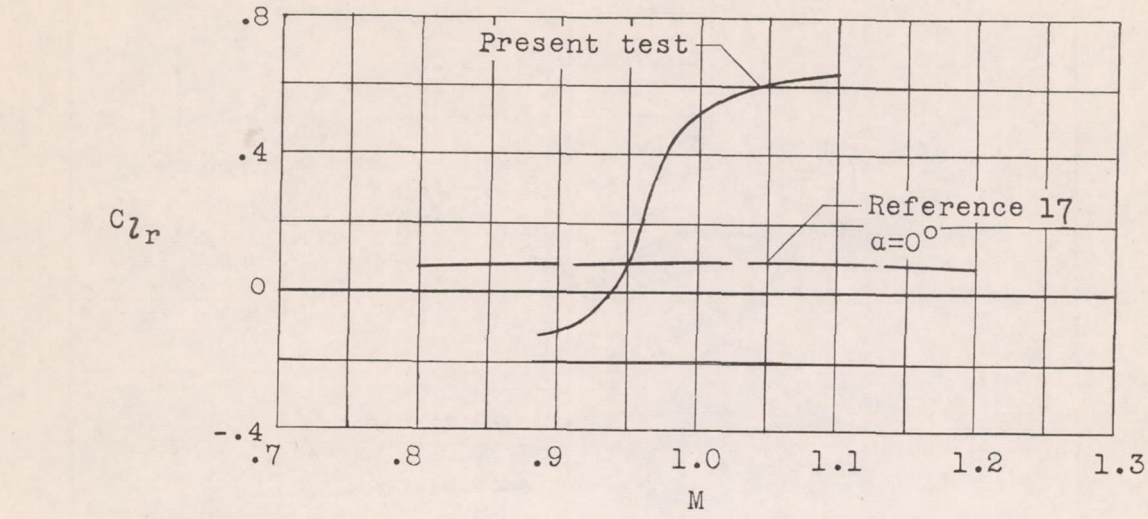


Figure 17.- Comparison between experimental and predicted variation of sideslip stability derivatives.



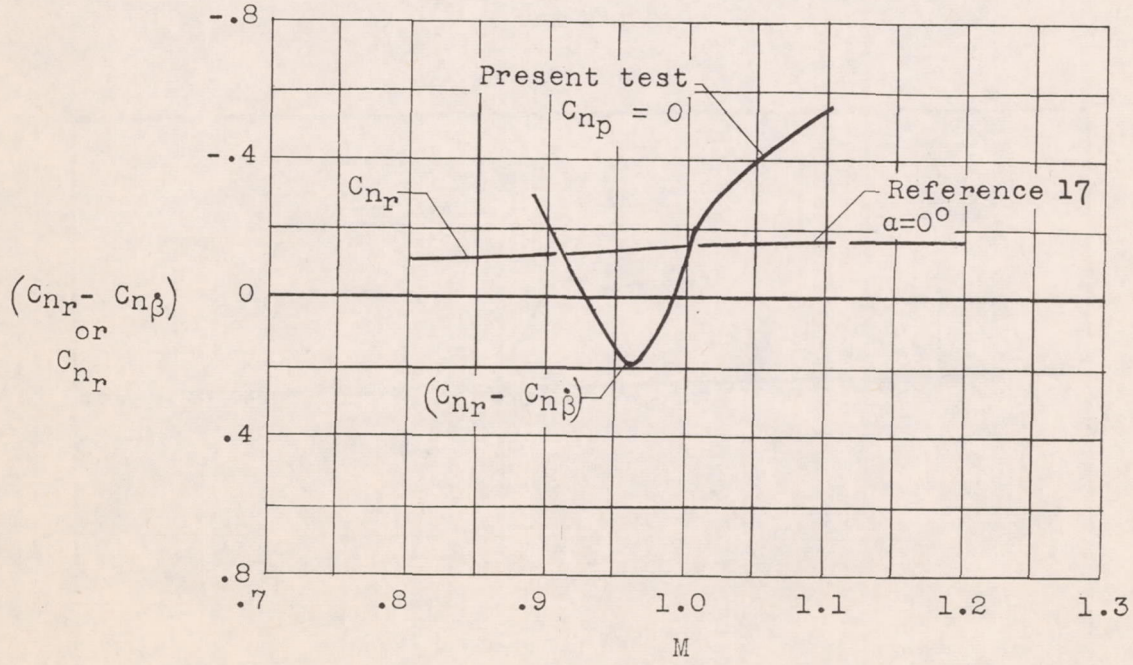


Figure 18.- Comparison between experimental and predicted variation of moment derivatives due to yawing.

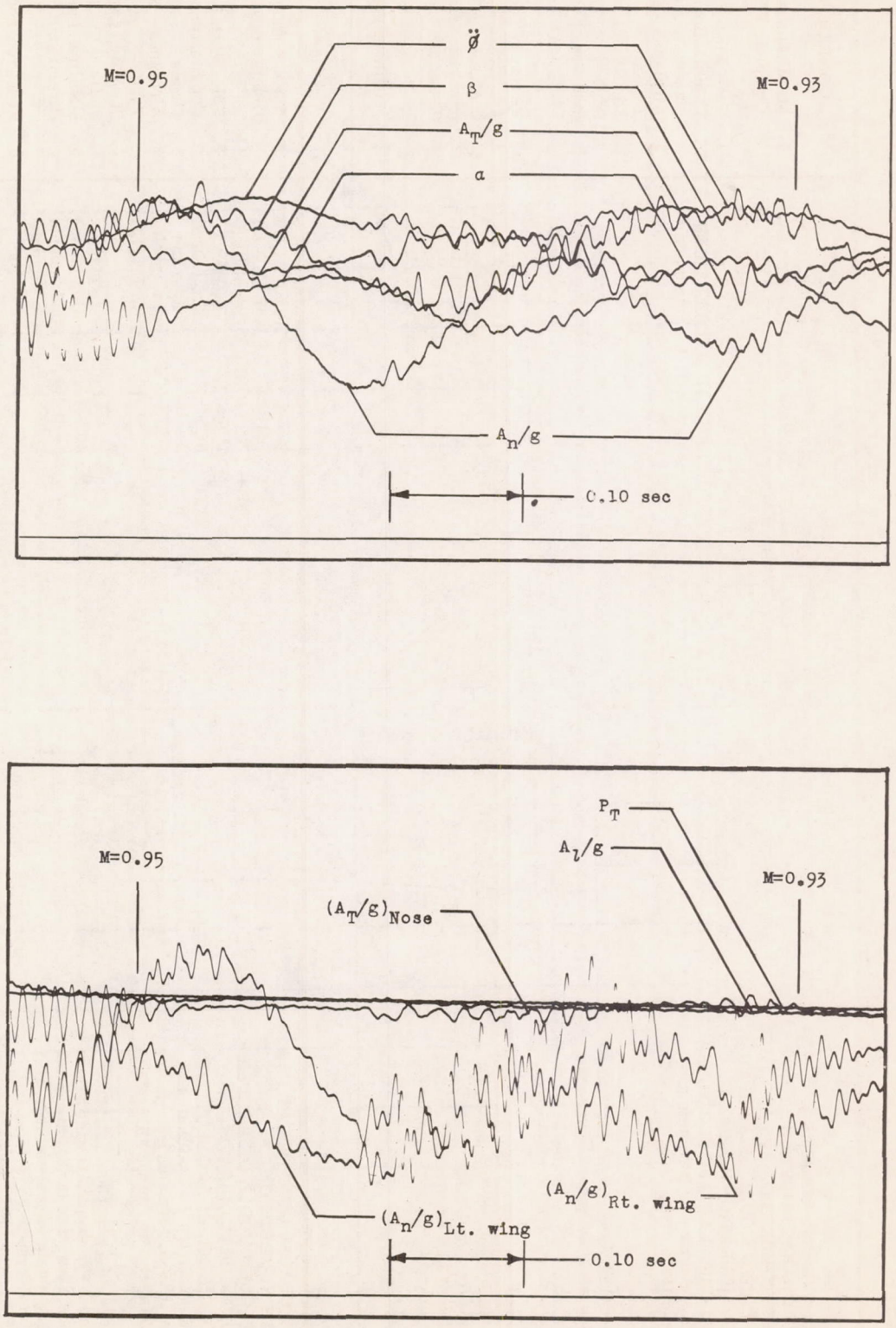


Figure 19.- Portion of telemeter record showing high-frequency and random oscillations.

NACA-Langley - 4-28-55 - 325